

An information-theoretic approach to the gravitational-wave burst detection problem

Ryan Lynch,* Salvatore Vitale, Reed Essick, and Erik Katsavounidis
Massachusetts Institute of Technology, 185 Albany St, 02139 Cambridge USA

Florent Robinet
LAL, Université Paris-Sud, IN2P3/CNRS, F-91898 Orsay, France

The advanced era of gravitational-wave astronomy, with data collected in part by the LIGO gravitational-wave interferometers, has begun as of fall 2015. One potential type of detectable gravitational waves is short-duration gravitational-wave bursts, whose waveforms can be difficult to predict. We present the framework for a new detection algorithm – called *oLIB* – that can be used in relatively low-latency to turn calibrated strain data into a detection significance statement. This pipeline consists of 1) a sine-Gaussian matched-filter trigger generator based on the Q-transform – known as *Omicron* –, 2) incoherent down-selection of these triggers to the most signal-like set, and 3) a fully coherent analysis of this signal-like set using the Markov chain Monte Carlo (MCMC) Bayesian evidence calculator *LALInferenceBurst* (LIB). These steps effectively compress the full data stream into a set of search statistics for the most signal-like events, and we use elements from information theory to minimize the amount of information regarding the signal-versus-noise hypothesis lost during this compression. We optimally extract this information by using a likelihood-ratio test (LRT) to map these search statistics into a significance statement. Using representative archival LIGO data, we show that the algorithm can detect gravitational-wave burst events of realistic strength in realistic instrumental noise with good detection efficiencies across different burst waveform morphologies. We also demonstrate that the combination of search statistics by means of an LRT can improve the detection efficiency of our search. Finally, we show that oLIB’s performance is robust against the choice of gravitational-wave populations used to model the LRT likelihoods.

I. INTRODUCTION

Detection of gravitational waves (GWs) with advanced ground-based detectors has never been closer. The two Advanced LIGO detectors [1] began their first observing run in September 2015, and Advanced Virgo [2] is expected to join them in 2016. These advanced detectors join GEO 600 [3] and through a sequence of commissioning periods, the advanced detectors are expected to reach their design sensitivities within the next 3-4 years [4]. Two additional instruments, LIGO India [5] and the Japanese Kagra [6] should join the global network before the end of the decade, further increasing our sensitivity to GWs.

These instruments have many potential sources. Some, such as the inspiral and merger of stellar remnants, known as compact binary coalescence (CBC), have well-modeled and well-understood theoretical waveform predictions [7]. With these models in hand, Weiner matched-filtering techniques provide optimal ways to detect the known waveform. Tremendous theoretical effort has gone into improving these models and providing reliable approximants throughout the most interesting parts of parameter space. However, there are other types of GW sources with poorly modeled or unknown waveforms, such as core-collapse supernovae [8–12]. This paper focuses on short duration (≤ 1 second) unmodeled transients with frequencies between ten Hz and a few kHz,

commonly known as GW bursts. Therefore, throughout this paper we make the assumption that the targeted signals are inherently unknown in origin and morphology, although searches for unmodeled bursts are indeed sensitive to better understood sources [13].

Discovering unmodeled sources of GWs is an exciting prospect for the advanced detectors. In particular, localizing generic sources in the sky [14] could provide information about their origin and accurate reconstruction of the waveform could determine the mechanism behind supernovae [15]. However, before this information is available or believable we must ensure that we have confidently detected a GW signal. In this way, we can separate parameter estimation and inference from detection. This paper focuses on detection and presents a new pipeline – called *oLIB* – that generates significance estimates for GW candidates via nearly-lossless compression of the information contained in the raw data.

Many different burst detection statistics and schemes have been proposed in the past [16–21]. In particular, another pipeline [22, 23] has recently claimed the ability to make high-confidence detections [21] using the Bayesian evidence computed by a stochastic sampler as a follow-up to other searches, much like how oLIB’s coherent step follows an incoherent analysis (see §II). It is of great interest to have overlap between independent search algorithms so that cross-validation can be carried out for detection candidates. Although most detection schemes are similarly motivated by noise models for our detectors, typically assumed to be stationary and Gaussian, there is uncertainty regarding how optimal their exact statis-

* ryan.lynch@ligo.org

tics are for unmodeled bursts in real detector noise. oLIB presents a way to algorithmically and independently generate optimal search statistics for proposed signal and noise hypotheses through an application of information-theoretic concepts. Furthermore, it compresses these data streams into a single scalar detection statistic instead of a vector of search statistics, which removes the arbitrariness of placing thresholds that can affect other multi-statistic pipelines. This compression is done in such a manner that it minimizes the information lost concerning the signal-versus-noise hypothesis. This process is carried out by first selecting a subset of data containing excess power that is obtained through a time-frequency decomposition based on the Q-transform [24–26], which we will refer to as *Omicron*. This step is followed by an incoherent coincidence between multiple detectors. The set of most “signal-like” incoherent coincidences are handed to a coherent follow-up, performed with LALInference Burst (LIB) [14, 27, 28], which compresses the data into search statistics. Applying a likelihood-ratio test (LRT) to these search statistics produces a scalar search statistic, which is then mapped into a significance estimate. At each step in the pipeline, we take care to analyze possible losses of information, which include modeling uncertainty and/or waveform mismatch, among other sources.

While the signals oLIB targets are inherently unknown, the pipeline makes some assumptions about their morphology. However, we demonstrate that the detection efficiency for any given morphology is not strongly influenced by which morphology we use to train oLIB. This shows that oLIB is robust against mismatches between the assumed signal population and the actual signal population, allowing us to approximately quantify any systematic sub-optimality due to poor assumptions about signal populations. We also quantify how well oLIB can recover different GW morphologies. While oLIB is more sensitive to signals that better match its assumptions, it can still detect signals that differ significantly from its internal models at astrophysically relevant signal strengths. Furthermore, these robust detection statements can be reached in real time, allowing oLIB to inform the rapid follow-up of GW candidates, if not initiate the follow-up itself.

We describe oLIB’s algorithmic structure in more detail in §II, focusing on the information theoretic justification of our design choices in §II A. We present the incoherent trigger generation in §II B and incoherent coincidence tests in §II C. §II D describes the coherent analysis using LIB and §II E discusses the LRT and how it is used within oLIB. Using archival (public) LIGO data, we present an example analysis in §III. This includes a description of a hierarchical method of estimating oLIB’s background in §III C and the distributions of the detection statistics used to form the likelihood ratio in §III B. We conclude in §IV and provide many technical details in the Appendix.

II. ALGORITHM DESCRIPTION

In this section, we describe the workflow within oLIB and justify the design choices at each step. The pipeline is graphically depicted in Fig. 1. A general motivation is provided in §II A, and the specific steps in the pipeline are described afterward. §II B describes the Omicron trigger production and §II C describes the incoherent coincidence requirements and down-selection. We describe the LIB coherent follow-up in §II D and describe the LRT used to determine a trigger’s significance in §II E 1.

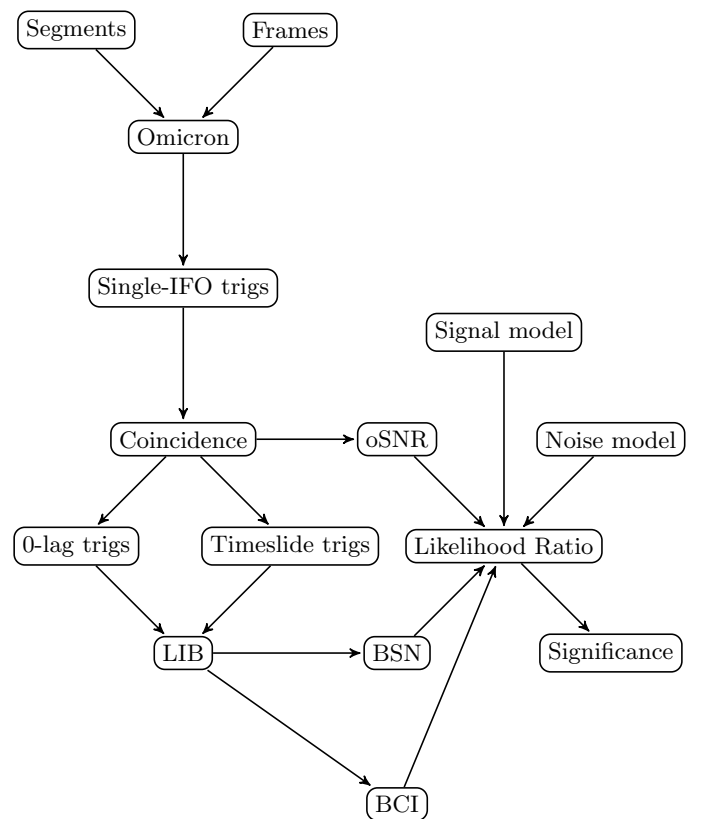


FIG. 1. A flow chart illustrating the hierarchical structure of the oLIB pipeline. Calibrated strain data and time segments are fed into Omicron, which produces single-interferometer triggers. The triggers are down-selected via incoherent clustering, data-quality vetoes, and coincidence. Sets of the most significant foreground (0-lag) and background (timeslide) events are passed onto LIB. The Bayes factors produced by LIB (BSN, BCI) and Omicron’s estimate of the SNR (oSNR) are combined using an LRT. The LRT also requires likelihood models for both the detection (signal) and non-detection (noise) hypotheses. Finally, the LRT provides a measure of the foreground events’ detection significance (a false-alarm rate (FAR)).

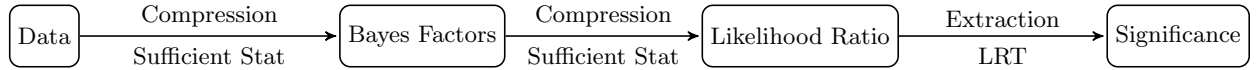


FIG. 2. Schematic of how information is compressed into a significance estimate within the oLIB pipeline. Ideally, sufficient statistics allow for lossless data compression, and the LRT allows for optimal information extraction.

A. Information-theoretic justification of pipeline design

While we have motivated the design of the oLIB pipeline with the idea of preserving information, we have yet to rigorously define this concept. We will briefly introduce these ideas here, but derivations can be found in Appendix A. First, we quantify this qualitative concept by utilizing elements from information theory, defining the information in the data stream \vec{x} regarding the signal-versus-noise binary hypothesis H as their mutual information

$$I(H; \vec{x}) = \mathcal{H}(H) - \mathcal{H}(H|\vec{x}) \quad (1)$$

where $\mathcal{H}(H)$ and $\mathcal{H}(H|\vec{x})$ are the entropy and conditional entropy, respectively, of the probability distributions for H (see Appendix A 2 a for explicit definitions of entropy). Because entropy is a measure of distributional uncertainty, the information $I(H; \vec{x})$ quantifies how the uncertainty in the true hypothesis H is reduced by knowledge of the data \vec{x} .

Now that information is defined, we wish to see how it changes when we compress the data vector \vec{x} into a search statistic $t(\vec{x})$. As proved in Appendix A 2 a, the Data Processing Inequality states that compressing a data vector into a search statistic can only reduce or preserve the amount of accessible information regarding the true hypothesis H :

$$I(H; \vec{x}) \geq I(H; t(\vec{x})). \quad (2)$$

Also shown in Appendix A 2 a, the Data Processing Inequality becomes an equality for a certain class of statistics (sufficient statistics). A statistic $t(\vec{x})$ is sufficient if and only if it satisfies the relationship

$$P_{H|x}(H|\vec{x}) = P_{H|t}(H|t(\vec{x})), \quad (3)$$

which implies that identical inference can be done with both \vec{x} and $t(\vec{x})$.

The key design feature in our search is that, for binary hypothesis testing like our signal-versus-noise test, the likelihood ratio

$$\Lambda(\vec{x}) \equiv \frac{P_{x|H}(\vec{x}|\text{signal})}{P_{x|H}(\vec{x}|\text{noise})} \quad (4)$$

is a sufficient statistic. We emphasize that likelihood ratios only compress data losslessly when the likelihoods used in the ratio are the true likelihoods of the possible hypothesis realizations. This scenario commonly breaks

down in two ways. First, the hypothesis used in the likelihood might not be exactly H . An example is when the signal hypothesis refers to a GW being present, but with the wrong waveform morphology. Second, the functional form of the probability distributions $P_{x|H}$ might be incorrect. In either case, as long as the “best-fit” likelihood ratio is a good approximation to $P_{x|H}(\vec{x}|H)$, we expect this loss to be minimal.

We now explore how to utilize the sufficiency of the likelihood ratio. By construction, the Bayes factor $B_{i,j}$ computed for any two hypotheses H_i and H_j , where

$$B_{i,j} \equiv \frac{P(\vec{x}|H_i)}{P(\vec{x}|H_j)}, \quad (5)$$

is a likelihood ratio and in turn a sufficient statistic. Thus, compressing the data vector into a Bayes factor is lossless as long the two hypotheses perfectly describe all possible data realizations. Nevertheless, there might be multiple model classes for both signals and noise within the broader signal-versus-noise hypotheses, with each representing a different data realization. For example, GW burst signals can have varying morphologies, and the detector noise may behave as either Gaussian or non-Gaussian (“glitchy”) noise [29]. We can compute Bayes factors for each of these model class hypotheses, but then we need a way of losslessly combining the information contained within each model class hypothesis about the overall signal-versus-noise hypothesis. If we treat the set of Bayes factors for each model class hypothesis as another data vector \vec{x}_B , then further compression of the data into the likelihood ratio

$$\Lambda(\vec{x}_B) \equiv \frac{P(\vec{x}_B|\text{signal})}{P(\vec{x}_B|\text{noise})} \quad (6)$$

is lossless (see Fig. 2).

There is still the question of what happens when no model class hypothesis perfectly describes the true signal-versus-noise hypothesis. If this is the case, the compression is lossy. Furthermore, it isn’t clear what happens if we combine lossy search statistics. Fortunately, one can show that including another data point \vec{x}_+ into a data vector can only increase the information contained about the hypothesis H :

$$I(H; \vec{x}, \vec{x}_+) \geq I(H; \vec{x}). \quad (7)$$

Thus, we can combine lossy search statistics with lossless search statistics without losing information, and we can losslessly compress the information contained within lossy search statistics, both by means of a likelihood ratio. We stress that even though information might have

been lost in compressing data from \vec{x} to \vec{x}_B , further compression can still be lossless.

It should be noted that, to this point, we have only discussed minimizing the loss of information when compressing data. However, all of this lossless compression is useless if we do not have an optimal way of extracting the information from the compressed data. As an illustrative example, note that the uncompressed data streams contain the maximal amount of information concerning H , but just having this maximal amount of information does not guarantee that any arbitrary estimator \hat{H} will be optimal. Fortunately, the Neyman-Pearson lemma [30] argues that an LRT maximizes the probability of signal detection at a given false-alarm probability, so it is an optimal means of information extraction. As we will see in § II E, once we have a likelihood ratio, evaluating an LRT is straightforward.

With this information-theoretic justification in mind, the general structure of oLIB is as follows:

1. Use Omicron to flag stretches of the detector’s data streams that contain excess power.
2. For each trigger, use LIB to calculate Bayes factors across all signal and noise model classes. If the set of signal and noise model classes perfectly describes every data realization, then the compression is lossless. If not, information loss is introduced.
3. For each trigger, use a likelihood ratio Λ to combine the information contained within all of the model classes’ Bayes factors. As long as the signal and noise likelihoods used to compute the likelihood ratio are the true likelihoods for each model class, the compression from a set of Bayes factors to Λ is lossless.
4. Extract the information contained by Λ regarding H using an LRT to map Λ into a significance statement

In the following sections, we describe these steps in greater detail.

B. Omicron

Omicron provides fast and accurate identification of statistically significant deviations from Gaussian noise in a single interferometer’s data stream. It is based on the Q transform, which varies the duration of data used within a Fourier transform to maintain a constant quality factor $Q \propto \tau \cdot f_0$, meaning the duration τ is inversely proportional to the targeted frequency f_0 [24–26]. By repeatedly decomposing a data stream into several planes of constant Q, Omicron can search for excess power with different characteristic aspect ratios in the time-frequency plane. In effect, the Q transform is similar to matched-filtering with a bank of sine-Gaussian waveforms, each

of which has a characteristic shape in the time-frequency plane and is well-localized.

While any given signal may “ring up” multiple templates, clustering and post-processing collate the large number of triggers into a subset describing the most prominent features of each transient signal. Clustering can be performed within Omicron, but we elect to use the full, unclustered trigger stream in oLIB. Instead of relying on Omicron to cluster triggers, we develop our own clustering and coincidence algorithm, described in § II C. In this way, oLIB only uses Omicron to flag interesting stretches of data and performs all of the down-selection outside of the Omicron processes.

C. Incoherent Coincidence

As mentioned, Omicron matched-filters a bank of sine-Gaussian templates with the entire stretch of data. Any template that “rings up” with a signal-to-noise ratio (SNR) greater-than-or-equal-to a threshold value is recorded as an Omicron trigger. A threshold value of 5.5 is standard in our analysis. These triggers denote an excess of signal power in an individual detector’s data stream at a given time. However, the presence of excess power alone does not provide strong evidence of a GW as it can also be generated by loud noise fluctuations, or “glitches”. Furthermore, many of the triggers provide redundant information. For example, an excess of power in the data stream can have significant overlap with multiple sine-Gaussian templates, so there are routinely multiple templates of different f_0 and Q recorded at identical times in the data stream. Unfortunately, LIB is too computationally expensive to follow-up all of the Omicron event triggers on reasonable timescales, so some sort of incoherent down-selection must be done, where only the most “GW-like” signals are passed onto LIB.

The form of the down-selection naturally falls out of how we define “GW-like”. Even though the oLIB pipeline is designed to detect unmodeled GW bursts, we hypothesize that detectable burst signals exhibit several qualities. More precisely, we expect the same wave to interact with all detectors, which leads us to expect specific signatures to be left in the data streams of all detectors. Omicron models these signatures as single sine-Gaussians, so we hypothesize that the triggers produced by a single burst-like GW will cover similar ranges of f_0 and Q in each detector. In addition, from General Relativity, we expect GWs to travel at the speed of light, meaning there is a given time window, defined by the physical separations of the detectors, in which GWs can interact with each of the detectors. As a result, we choose to pass LIB only the Omicron event triggers whose f_0 and Q values are identical across all detectors and whose detection times are consistent with this time-of-flight time window (although we note that requiring *exact* f_0 and Q match instead of *close* f_0 and Q match may result in a loss of some quieter signals or broadband signals whose SNRs

are diluted across large regions of time-frequency space).

With this definition of “GW-like” in mind, our exact down-selection takes the following form. First, for each individual detector, we form “clusters” of Omicron triggers with identical f_0 and Q that are spaced closely in time. More precisely, we open an acceptance gate at the detection time of a trigger with given f_0 and Q, and we leave the gate open so long as a trigger of identical f_0 and Q is found within the time interval $\Delta t_{\text{cluster}}$, closing it otherwise. Each continuous stretch of acceptance is defined as a “cluster” for a template, and we down-select each cluster to the loudest SNR trigger contained within it. The $\Delta t_{\text{cluster}}$ used in our analyses is 100 ms, though the analysis results are relatively invariant for time windows of similar size.

We then take this set of clustered triggers (i.e., the representative loudest-SNR trigger of each cluster) for each detector. The search pipeline also has provisions for the inclusion of data-quality and veto flags as established by the LIGO and Virgo collaborations [29, 31, 32]. These vetoes are informed by the detectors’ auxiliary channels in order to determine whether the excess power in the detectors is caused by environmental, instrumental, or other non-astrophysical sources of noise instead of a flux of GWs. To be consistent with published transient searches by the LIGO-Virgo collaborations over the data sample we have used to benchmark our detection algorithm [16], we remove all clustered triggers that fall within these vetoed times.

Next, we take the set of surviving clustered triggers and apply a “loose” coincidence restriction among the detectors for event triggers of identical f_0 and Q. More precisely, we only keep clustered triggers of the i^{th} detector that have a clustered trigger counterpart of identical f_0 and Q in the j^{th} detector, requiring corresponding times to fall within a time window $\Delta t_{\text{coin},ij}$. This coincidence is considered “loose” because the value of $\Delta t_{\text{coin},ij}$ is greater than the exact time-of-flight window between the two detectors (i.e., we typically choose $\Delta t_{\text{coin},HL}$ to be 50 ms, while the exact time-of-flight window is closer to 10 ms). For each of these loosely coincident event triggers, we calculate a network SNR $\rho_{\text{net}}^2 = \sum_{i \in \text{Detectors}} \rho_i^2$.

Penultimately, we take this set of loosely coincident triggers and require “strict coincidence” using an LRT. The details of this LRT are explained more explicitly in § II E, but we can paint the general picture here. We can define a set of coincidence parameters $\vec{\theta}_{\text{coin}}$ based on the parameters provided by Omicron, such as $\Delta t_{\text{coin},ij}$, f_0 , Q, SNR_{net}, etc.. We then calculate the signal-versus-noise likelihood ratio at the coordinate $\vec{\theta}_{\text{coin}}$, defining our “strictly coincident” event triggers as those that exceed a threshold likelihood-ratio value.

Finally, we cluster this set of strictly coincident triggers one last time so there is at most one trigger per LIB analysis window, Δt_{LIB} , thus avoiding redundant LIB runs. We do this by iteratively keeping the loudest SNR trigger in a set of non-overlapping intervals of length Δt_{LIB} until all LIB triggers are separated by at least Δt_{LIB} . This

set of LIB-clustered, strictly-coincident triggers is passed onto LIB.

D. LIB

LALInferenceBurst is based on LALInference [28], a Bayesian parameter estimation and model selection algorithm. While LALInference assumes that the model waveform is produced by a CBC system (any pairwise combination of a neutron star and a black hole), LIB can work with short duration signals such as sine-Gaussians, Gaussians and damped sinusoids.

The standard configuration of oLIB uses LIB with sine-Gaussian templates. These templates depend on 9 parameters: central frequency f_0 , quality factor Q, amplitude (the parameter actually used is the h_{rss} , see [14]), time, phase, sky position, polarization angle, and eccentricity.

LIB uses the nested sampling algorithm [33] to efficiently sample the 9-D parameter space. N “live points” are evolved by sampling the prior distribution in order to calculate the Bayesian evidence $P_{x|H}(\vec{x}|H)$ for the data stream \vec{x} and hypothesis H. For oLIB, we use the default termination condition [27] that the extra Bayesian evidence one would lose if all of the live points had a likelihood equal to the maximum-likelihood point found is smaller than 0.1.

As shown in Eq. 5, the evidences calculated by LIB can be used to construct two Bayes factors. This first compares a signal model (a coherent sine-Gaussian GW is present in the data) to a Gaussian-noise model (only Gaussian noise is present in the data), and we refer to it as BSN. Another compares the same signal model to an incoherent noise-glitch model (incoherent sine-Gaussian signals of non-GW origin are present in each instrument), and we refer to it as BCI. The reader is directed to [27, 28] for more details about nested sampling and these Bayes factors (the Bayes factors are also described in greater detail in Appendix A 2 e). As a by-product, LIB produces posterior distributions for all 9 parameters on which the model waveform depends. While some of them might not be of immediate use since the GW signal may not necessarily be well-matched by a simple sine-Gaussian, it has been shown that the sky position of the source, as measured by LIB, can be used for electromagnetic follow-up [14].

E. Likelihood Ratio Test

We now explore how to use an LRT to extract information from our search statistics and how to train this LRT.

1. Using the Likelihood Ratio Test for Detection

The primary purpose of oLIB is to optimally extract the information contained within the data regarding the signal-versus-noise hypothesis and to use this information to inform a detection statement. This extraction is aided by first compressing the data into a set of search statistics. As we argue in § II A, our working assumption is that the Bayes factors produced by LIB contain a sufficiently large percentage of the information contained within the raw data streams. However, even though Bayes factors allow for lossless compression if they span hypothesis models containing the true hypotheses, Eq. 7 ensures us that adding any search statistics to our vector of search statistics can only increase the information we have at our disposal. With any n-dimensional set of statistics $\vec{x} = x_0, x_1, \dots, x_n$ we decide to use in our analysis, the detection problem is equivalent to optimally extracting this information.

This problem immediately suggests the use of an LRT. The motivation stems from the Neyman-Pearson lemma [30], which states that the LRT is the optimal method of binary hypothesis testing in that it maximizes the probability of successfully detecting a signal at a given false alarm probability (see Appendix A 1 for a proof and further discussion of the Neyman-Pearson lemma). The exact form of the LRT for the signal-versus-noise binary hypothesis testing is

$$\Lambda(\vec{x}) \equiv \frac{P_{x|H}(\vec{x}|\text{signal})}{P_{x|H}(\vec{x}|\text{noise})} \stackrel{\text{signal}}{\gtrless} \stackrel{\text{noise}}{\lessgtr} \alpha \quad (8)$$

where $\Lambda(\vec{x})$ is the value of the likelihood ratio at a coordinate \vec{x} , $P_{x|H}(\vec{x}|\text{signal})$ and $P_{x|H}(\vec{x}|\text{noise})$ are the likelihood distributions of getting the coordinate point \vec{x} , and α is a threshold value of the likelihood ratio. Thus, if $\Lambda(\vec{x})$ is greater than the threshold, we decide that there is a signal present in the data with a false-alarm rate (FAR) set by α (the procedure for establishing a FAR is addressed later in this section). Eq. 8 essentially uses the likelihoods to divide our search statistic parameter space \mathcal{X} into regions of detection and non-detection, with α determining the boundary.

We emphasize that the LRT allows us to optimally compress the n-dimensional vector of search statistics \vec{x} into a *single scalar measure of significance* $\Lambda(\vec{x})$. While several GW searches attempt to combine information from multiple search statistics [16, 21], only a few [34–36] utilize the optimality of the LRT. The LRT has the property of optimally ranking events because the FAR is a monotonically decreasing function of $\Lambda(\vec{x})$ (proof in Appendix A 1). Thus, the triggers with the largest values of $\Lambda(\vec{x})$ are necessarily the most signal-like triggers encountered. This monotonicity allows us to optimally extract information concerning the signal-versus-noise hypothesis from our search statistics, and it immediately suggests the following method for determining the significance of our foreground with respect to our background.

The oLIB pipeline is run end-to-end on a stretch of background data, producing a vector of search statistics $\vec{x}_{\text{back},i}$ for each trigger i that is produced in the incoherent analysis (see § III A). Background estimation for GW detectors is complicated by the fact that it is impossible to isolate the detectors from any incident GW flux, meaning GWs are always present in the detectors' data streams, even if they reside below the detector noise floor. Nevertheless, we can transform a stretch of data into a stretch of data without any *coherent* GWs by a technique known as data time-shifting [37]. In effect, we shift the timestamps of one detector's data stream in bulk (i.e., we apply the same time shift to every discrete time sample) with respect to another detector's data stream before doing coincidence. If this timeshift is greater than the hypothesized time-of-flight between the detectors for a GW, then there can be no coherent signature of the GWs in our data streams. Thus, any triggers found in coincidence in the two detectors can be modeled as non-Gaussian (commonly Poisson-distributed) noise artifacts independently occurring simultaneously in the detectors. Thus, timeslides provide a method for approximating the noise-only background coincidence rate of our detectors using real detector data (although, to be sure, there are subtleties involved regarding whether or not to remove 0-lag coincidences before performing the timeslides).

With this background data set in hand, we calculate a value of the likelihood ratio $\Lambda(\vec{x}_{\text{back},i})$ for each background event trigger i . This calculation effectively assigns a significance ranking to each of the background triggers. Using the total coincident livetime of our background analysis (i.e., the duration of time during which a trigger could have been produced), we can approximate the FAR of a threshold α with a simple counting experiment:

$$\text{FAR}(\alpha) \approx$$

$$\frac{\text{No. of background events with } \Lambda(\vec{x}_{\text{back},i}) \geq \alpha}{\text{Total coincident livetime of background analysis}} \quad (9)$$

Finally, for any foreground trigger j (i.e., any trigger produced in an analysis with no timeslides performed, commonly referred to as “0-lag” triggers), the oLIB pipeline produces a vector of search statistics $\vec{x}_{\text{fore},j}$. By calculating the likelihood ratio $\Lambda(\vec{x}_{\text{fore},j})$ and setting $\Lambda(\vec{x}_{\text{fore},j}) = \alpha$, we can use Eq. 9 to estimate the FAR at which the foreground trigger j can be considered a detection.

We stress again that while this LRT-based method is straightforward and can be considered optimal under several criteria (information preservation and extraction), all optimality statements assume we have access to the true likelihood distributions for both our signal and noise hypotheses. Any inaccuracies in our likelihoods will lead to both lossy compression and sub-optimal information extraction. Thus, we need to accurately model these likelihood distributions before we undertake any estimation of event significance, a process which we will refer to as “training” the LRT.

2. Training the Likelihood Ratio Test

In order to evaluate a trigger’s likelihood-ratio for a given set of search statistics \vec{x} , we need models for both the signal and noise likelihoods, $P_{x|H}(\vec{x}|\text{signal})$ and $P_{x|H}(\vec{x}|\text{noise})$, respectively. One approach to modeling the likelihood would be to analytically predict the distributions of the search statistics \vec{x} produced by the oLIB pipeline for both signal and noise triggers, thus producing theoretical models of $P_{x|H}(\vec{x}|\text{signal})$ and $P_{x|H}(\vec{x}|\text{noise})$. Such an approach definitely has advantages. Specifically, it could require minimal computational resources to implement. However, obtaining accurate theoretical models of these distributions is non-trivial. We instead choose to implement a more straightforward, empirical approach to our modeling: “training” the likelihoods. By “training” we mean simulating large sets of signal and noise triggers, calculating the vector of the search statistics \vec{x} for each trigger, and fitting the likelihood distributions using the resulting set of vectors. In order to turn the empirical set of search statistic vectors into likelihood models, we use non-parametric regression, namely Gaussian kernel density estimation (KDE), described in detail in Appendix B.

As mentioned in § III A, because we are treating GW bursts as unmodeled, we need to enforce a set assumptions in order to distinguish GW signals from noise. Although, we can obtain populations of noise triggers through timeslides, we must make assumptions regarding the true nature of GW burst signals in order to obtain a population of signal triggers. These assumptions involve selecting the set of signal morphologies on which to train (e.g., sine-Gaussian signals) and then specifying the distribution of these morphologies’ intrinsic parameters (e.g., the distributions of f_0 and Q for sine-Gaussian signals). There are also extrinsic parameters distributions, such as the source sky location, but these distributions can be modeled and justified theoretically (e.g., uniformly in volume when considering far away sources), and thus they do not involve the same degree of arbitrariness as the signals’ morphologies and intrinsic parameters.

While the arbitrariness of selecting the signals’ intrinsic population may seem like a substantial limitation for oLIB, we show that the impact of training on different population models is actually quite small. We demonstrate this feature quantitatively (see § III C 3), but can outline an intuitive understanding as follows. Any coherent GW signal interacts with oLIB in a sufficiently different manner than incoherent noise coincidences, meaning we can train our LRT to distinguish coherent signals from incoherent noise regardless of the exact form of our training populations. Furthermore, because the evaluation of Eq. 8 amounts to merely evaluating two likelihoods at a point in parameter space \vec{x} , it is computationally inexpensive to evaluate a set of LRTs for several different population models once their likelihoods have been estimated. It is feasible to have several searches,

each trained on different source populations, that may be slightly more sensitive to different sources of GW bursts.

Finally, we emphasize the trade-off between the information gained by adding a search statistic to \vec{x} and the accuracy of our likelihood modeling. Although adding a search statistic can only increase the information contained within \vec{x} about the signal-versus-noise hypothesis, the increased dimensionality of the search-statistic parameter space becomes hard to model. KDE is very good at estimating the high-probability regions of a distribution where there are many training points, but it performs worse in low-probability regions of the distribution where there is a dearth of training points. Because increasing the dimensionality of a parameter space tends to quickly increase the volume where training points are sparse, adding a search statistic to \vec{x} can lead to modeling errors in the distribution’s tail unless the size of the training sets is correspondingly increased. Even though a vector of search statistics contains more information regarding the signal-versus-noise hypothesis, larger dimensionality can easily cause any further compression into a likelihood ratio to be lossy and any extraction of information with an LRT to be sub-optimal as a result of inaccuracies in the likelihood models.

III. APPLICATION TO HISTORICAL LIGO DATA

In order to test oLIB’s end-to-end performance, we simulated our own GW burst search on three days worth of data from the sixth science run of initial LIGO (S6). Specifically, we ran on science segments produced for the Hanford (H1) and Livingston (L1) detectors between 14-17 September 2010. These dates were chosen since they contain a blind chirp-like hardware injection [38] (removed from our analysis segments), and as a result this data has been thoroughly investigated [16, 29]. The science segments signify that the instruments were in proper states for observation, and additional data-quality vetoes generated by *hveto* [32] were applied to these segments during our incoherent down-selection.

This simulation involved running the pipeline in its entirety to extract a significance statement concerning possible detections. In order to ensure that we encountered a sufficient number of detection candidates, varying both in significance and morphology, we injected simulated GW waveforms into the data streams. These injections were taken from the S6 Burst injection set [16], and we injected them at multiple amplitude scale factors to ensure that a large range of SNRs were covered. We injected three morphologies: 1.) sine-Gaussians (SG), which oscillate sinusoidally in time within a Gaussian envelope and are characterized by a central frequency f_0 and a quality factor Q; 2.) Gaussians (GA), which consist of the Gaussian envelope alone and are characterized by their duration τ ; and 3.) white-noise bursts (WNB), which consist of random white noise within a Gaussian envelope and are

characterized by a starting frequency f_0 , a duration τ , and a bandwidth Δ . More detailed information regarding these burst morphologies can be found in [16] and [14].

To produce detection candidates, we ran oLIB end-to-end on the 0-lag data streams containing these injections. Additionally, we ran the pipeline on the data without any injections to obtain realistic estimates of the significance of the background. The results of both sets of runs are described in detail in the following sections.

A. Incoherent Results

We ran Omicron incoherently over both the H1 and L1 data streams, analyzing the frequency band spanning 64 to 2048 Hz. A lower single-detector SNR threshold of 5.5 was required for Omicron to record a trigger. Then, using the raw Omicron triggers, we clustered all identical-template triggers (as described in § II C) using a clustering window of $\Delta t_{cluster} = 100$ ms. We also removed vetoed livetime and triggers from our analysis at this clustering step.

Next, we performed identical-template coincidence using the coincidence window $\Delta t_{coin,HL} = 50$ ms in order to produce our foreground and background data sets. We produced our foreground using “0-lag” coincidence, meaning we performed the coincidence without shifting the data-streams with respect to each other in time. We produced our background using “timeslide” coincidence, meaning we performed timeslides before doing the coincidence. For this analysis, we performed two sets of timeslide coincidences. For our first set, we shifted the L1 data stream with respect to the H1 data stream 100 times, from -100s to 100s in 2s increments and imposed no network SNR restrictions (although the Omicron SNR threshold of 5.5 bounds the network SNR to be above $5.5\sqrt{2}$). For our second set, we shifted the L1 data stream with respect to the H1 data stream 2500 times, from -1250s to 1250s in 1s increments and required coincident event triggers to have a network SNR $\geq 6.5\sqrt{2}$. The reason we considered these two sets of timeslides is computational. Table I shows the trigger rate when using a network-SNR threshold of $5.5\sqrt{2}$ is more than an order-of-magnitude greater when using a network-SNR threshold of $6.5\sqrt{2}$. The non-negligible computational cost of our LIB analysis limits how many triggers we can follow-up within oLIB (we analyze the exact distribution of LIB runtimes in Appendix C). Therefore, if we can reduce the rate at which the incoherent step of the pipeline produces triggers, we can analyze a longer stretch of background and in turn make significance statements at lower false-alarm rates at fixed computational expense. Thus, as long as we can show that triggers with a network SNR $\leq 6.5\sqrt{2}$ are not likely to be our most signal-like significant background events, we can justify using the second set of timeslides to estimate our background in the low-FAR regime.

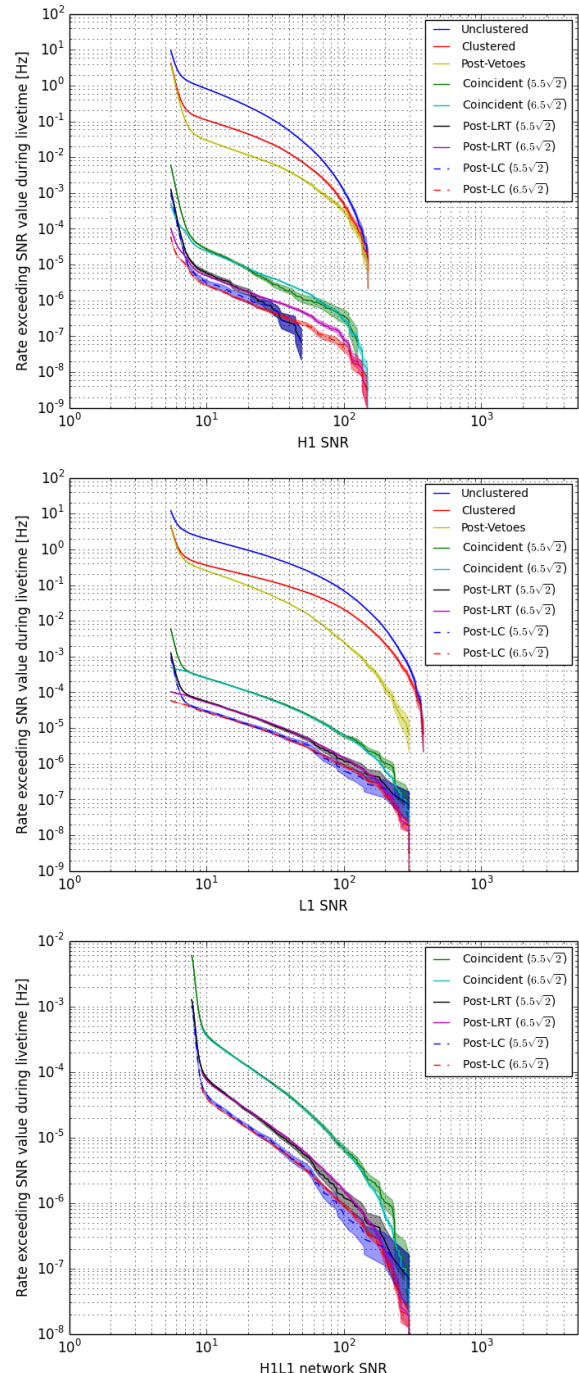


FIG. 3. The rates at which the triggers produced by Omicron exceed a given value of SNR. The top two plots give the trigger rate as a function of single-detector SNR, while the bottom plot gives them as a function of the network SNR. These event triggers are grouped by the down-selection steps they have just survived: either clustering, data-quality vetoes, “loose” timing coincidence, “strict” LRT coincidence, or LIB-window clustering (LC). Triggers surviving the coincident down-selection step are shown in two groups, those with lower-network-SNR thresholds of $5.5\sqrt{2}$ and $6.5\sqrt{2}$.

Finally, we apply a “strict coincidence” constraint to

TABLE I. Summary of the trigger rate at each step in the incoherent down-selection. The numbers given represent the set of triggers immediately after the quoted down-selection is applied.

Step	Number of Events	Total livetime (s)	Trigger Rate (Hz)
Unclustered H1	1410060	1.46×10^5	9.66
Unclustered L1	1786080	1.46×10^5	12.2
Clustered H1	623016	1.46×10^5	4.27
Clustered L1	676208	1.46×10^5	4.63
Clustered H1, post-Veto	585700	1.45×10^5	4.04
Clustered L1, post-Veto	630606	1.45×10^5	4.35
Coincident H1L1, network SNR cut $5.5\sqrt{2}$	85748	1.43×10^7	6.00×10^{-3}
Coincident H1L1, network SNR cut $6.5\sqrt{2}$	156344	3.15×10^8	4.96×10^{-4}
Post-LRT H1L1, network SNR cut $5.5\sqrt{2}$	18135	1.43×10^7	1.27×10^{-3}
Post-LRT H1L1, network SNR cut $6.5\sqrt{2}$	32779	3.15×10^8	1.04×10^{-4}
Post-LIB-clustering H1L1, network SNR cut $5.5\sqrt{2}$	14468	1.43×10^7	1.01×10^{-3}
Post-LIB-clustering H1L1, network SNR cut $6.5\sqrt{2}$	18599	3.15×10^8	5.90×10^{-5}

our coincident triggers by requiring them to survive a LRT using the H1-L1 time-of-arrival difference Δt_{HL} as the only coincidence parameter. Since the goal of this LRT is simply further down-selection, we set the threshold of this LRT to $\alpha = 1$, meaning an event trigger must have $P_{x|H}(\Delta t_{HL}|\text{signal}) \geq P_{x|H}(\Delta t_{HL}|\text{noise})$ to be considered strictly coincident. In effect, we only keep event triggers that are more likely signals than noise based on their value of Δt_{HL} . Finally, this final set of “strictly-coincident” triggers was clustered so that only one trigger was present per LIB analysis time-window of $\Delta t_{\text{LIB}} = 100$ ms.

The net result of our down-selection is illustrated in Table I and Fig. 3. Table I shows the total number of triggers, total livetime analyzed, and the total trigger rate at each step of the incoherent down-selection. Fig. 3 shows the rate at which triggers exceeding a given SNR occur in each step of the incoherent analysis for H1 and L1, respectively. From this data, we see that the clustering reduced the trigger rate by roughly a factor of 2-3, and, as expected, most of the discarded event triggers were low-SNR triggers that were clustered into high-SNR triggers. The application of data vetoes reduced the trigger rate by less than 10%, and removed low-to-medium SNR triggers for H1 and medium-to-high SNR triggers for L1.

The constraint of identical-template timing coincidence was responsible for our most significant reduction in trigger rate, lowering it by 3 and 4 orders-of-magnitude for lower-network-SNR thresholds of $5.5\sqrt{2}$ and $6.5\sqrt{2}$, respectively. This fractional reduction appears to be roughly constant, within errors, across all SNRs, which is consistent with a simple Poisson coincidence model (where $\text{rate}_{\text{coin}} \sim \text{rate}_1 \times \text{rate}_2 \times \text{coin window}$, and changing the single-detector SNR is equivalent to changing one of the single-detector rates). Again, we emphasize that the trigger rate falls steeply as a function of SNR, and raising the SNR threshold by 1 is responsible for an entire order of magnitude reduction of the trigger rate in our analysis. Although the backgrounds obviously differ in the regime between these lower-network-SNR thresh-

olds, they match each other within errors above these SNR thresholds, as we would expect, suggesting that the triggers are being produced at constant rates across all timeslides. The strict timing coincidence reduces the trigger rate by roughly a factor of 5, which is what is expected from simple Poisson coincidence estimates since the coincidence window is reduced by a factor of roughly 5 (from 50 ms for loose coincidence to ~ 10 ms for strict coincidence). Again, this factor of 5 reduction appears to remain constant, within errors, across SNR. Finally, the LIB clustering reduces the trigger rate by a factor of 1-2, which, characteristic of clustering, discards low-SNR triggers when they are clustered into high-SNR triggers.

In summary, the incoherent down-selection reduced the raw Omicron trigger rate by 4 and 5 orders-of-magnitude for lower-network-SNR thresholds of $5.5\sqrt{2}$ and $6.5\sqrt{2}$, respectively, meaning it reduced the computational cost of running the LIB portion of the oLIB pipeline by 4 to 5 orders of magnitude.

B. Coherent Results

For the coherent part of our analysis, we ran LIB over all triggers surviving our incoherent down-selection, both for the injection-filled foreground and the injection-free background. Our LIB runs used 256 live points and completed 256 MCMC jumps when generating new coordinates for the live points [27]. Our sampling frequency was 4096 Hz, and our priors were set to be uniform in volume, uniform between 64 Hz and 2048 Hz for central frequency, and uniform between 2 and 110 for quality factor. As described above, we analyzed two sets of timeslides with roughly the same amount of events: one with a lower-network-SNR threshold of $5.5\sqrt{2}$ and another with a lower-network-SNR threshold of $6.5\sqrt{2}$.

The distributions of the BCI and BSN for our background triggers are given in Figure 4, which shows the rate at which event triggers exceed different values of the Bayes factors. The distributions for both sets of timeslides agree within errors for large BSN (BSN $\gtrsim 10$),

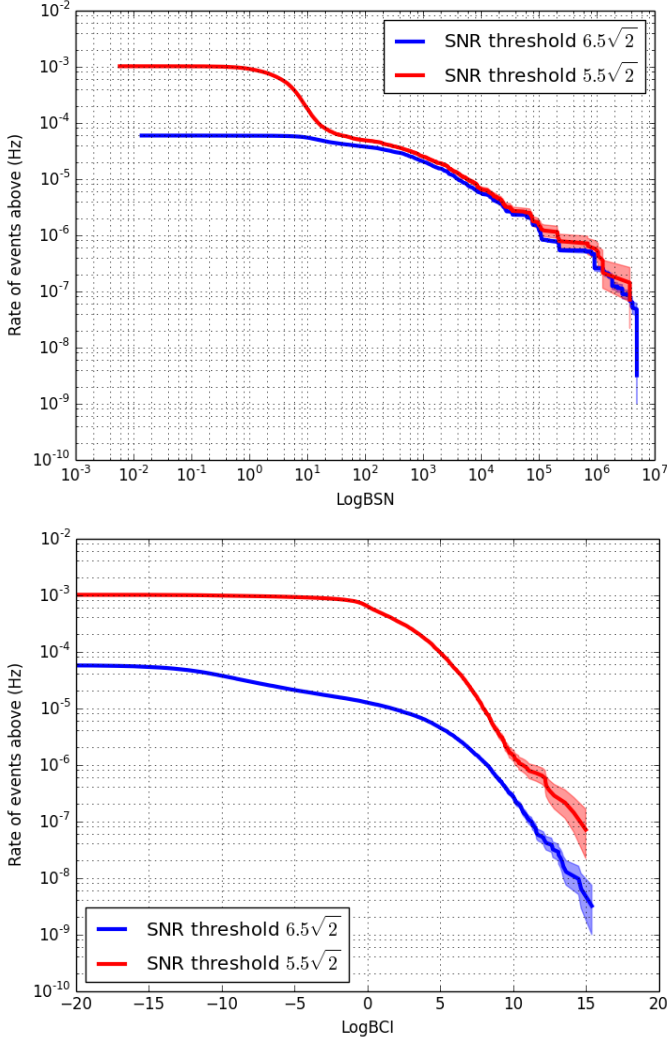


FIG. 4. The rate at which background triggers have Bayes factors exceeding a given value for BSN and BCI. The rates are given for the two sets of background triggers: those with lower-network-SNR thresholds of $5.5\sqrt{2}$ and $6.5\sqrt{2}$. The 68% confidence regions shown are derived from a binomial process with a uniform prior on the true rate.

but differ at small BSN ($BSN \lesssim 10$). This implies that triggers with an Omicron network SNR between $5.5\sqrt{2}$ and $6.5\sqrt{2}$ correspond to small-BSN events, which is expected since the BSN scales with SNR (one can easily show $\ln BSN \sim \frac{1}{2}SNR^2$ for data streams containing sine-Gaussian signals with high enough SNR that the noise is negligible). On the other hand, removing these low-SNR signals *does* affect the BCI distribution across all regimes. While the difference in rates between the two sets of timeslides is more severe at small BCI than at large BCI, this difference is still non-negligible at large BCI. Such behavior is not surprising since the BCI tests the coherence of the signal with signal amplitude largely normalized out. In summary, disregarding low-SNR event triggers only affects the low-magnitude regime of the BSN

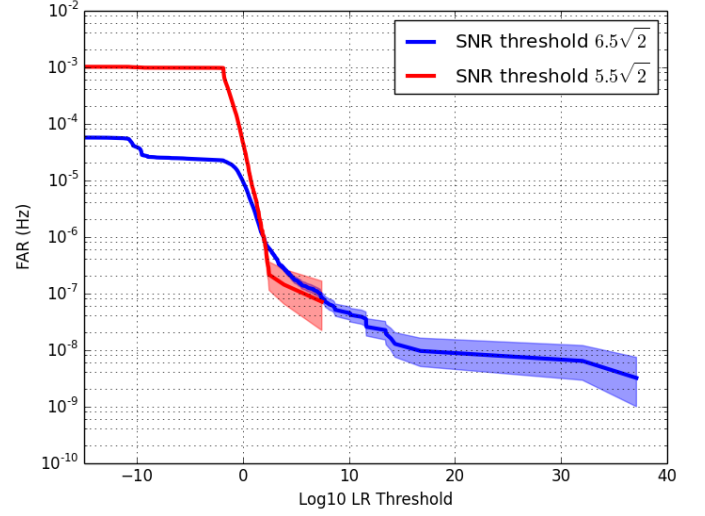


FIG. 5. The FAR achieved by setting a given likelihood-ratio threshold for detection. The LRT shown here is trained on both sine-Gaussian and white-noise burst signal populations and is evaluated using BCI and BSN as search statistics. The rates are given for the two sets of background triggers: those the lower-network-SNR thresholds of $5.5\sqrt{2}$ and $6.5\sqrt{2}$. The 68% confidence regions shown are derived from a binomial process with a uniform prior on the true rate.

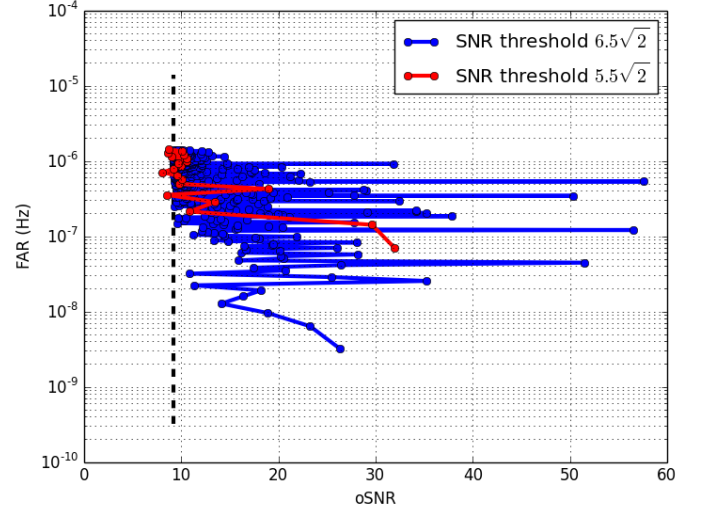


FIG. 6. The network SNR (oSNR) coordinates of the triggers as a function of their FARs. The points can be mapped into a likelihood-ratio threshold by matching FARs between this figure and Figure 5. Thus, the point with the lowest FAR has the highest likelihood ratio, and the lines connect neighboring likelihood ratios. The coordinates are given for the two sets of background triggers: those the lower-network-SNR thresholds of $5.5\sqrt{2}$ and $6.5\sqrt{2}$. The dashed vertical line marks the lower-network-SNR threshold of $6.5\sqrt{2}$.

distribution while it affects the BCI across all magnitude regimes.

With these Bayes Factor distributions, a question

arises as to whether or not we can estimate our background using a set of event triggers with *any* SNR threshold. By construction, we expect signals and signal-like noise event triggers to have large BSN and BCI. Underestimating the background rates in certain Λ regimes will cause us to overestimate the significance of detection candidates in that regime. Thus, we need to determine what regimes of our background Λ distributions are underestimated as a result of network SNR thresholds. Fig. 5 shows the rate at which background events above a certain value of Λ occur, i.e., the FAR, for both sets of analyzed timeslides. We see that the background rate in high-FAR and low- Λ regime is much higher for the SNR $5.5\sqrt{2}$ -thresholded background set than for the SNR $6.5\sqrt{2}$ -thresholded background set, which is expected because this is the low-BSN/low-BCI regime and, as seen above, we lose both low-BCI and low-BSN event triggers for network SNRs between $5.5\sqrt{2}$ and $6.5\sqrt{2}$. The distributions are plausibly consistent within errors for Λ between 0 and 10, though it must be noted that this regime of overlap is prone to small number statistic fluctuations since it is the tail of the $5.5\sqrt{2}$ -thresholded background set. What we would really like to see is the distribution of the $5.5\sqrt{2}$ -thresholded background set extended to the low-FAR and high- Λ regime, which is the regime where strong detection candidates would reside. If the distributions were consistent with one another in this low-FAR regime, then we could argue that our implementation of an SNR threshold had negligible effect on our background estimation in this regime. If the distributions were not consistent with one another, then we would know to what degree the $6.5\sqrt{2}$ -thresholded background set underestimated the background as compared to the $5.5\sqrt{2}$ -thresholded background set.

Nevertheless, extending the background set with lower-network-SNR threshold of $5.5\sqrt{2}$ to the same FAR as the background set with lower-network-SNR threshold of $6.5\sqrt{2}$ would require analyzing an order-of-magnitude more triggers, which in turns means an order of magnitude greater computational cost. Instead, we justify the distributional consistency in this low-FAR, high- Λ regime with the data we have. We emphasize that Figure 5 shows the distribution of background Λ for a likelihood ratio using the search statistics $\vec{x} = \{\text{BSN}, \text{BCI}\}$. Thus, the most signal-like background events will have both large BSN and BCI. Even though low-SNR events may have a large BCI, we expect these events to also have small BSN. This conflicting information will result in a smaller Λ than background events with both large BSN and large BCI, and we do not expect our SNR thresholding to discard high-BSN events. Figure 6 tracks the value of the Omicron network SNR as a function of FAR (which maps one-to-one to Λ , see Appendix A 1). We can see that for both sets of timeslides, the Omicron network SNR only reaches the threshold value of $6.5\sqrt{2}$ at FAR significance levels of $\gtrsim 10^{-7}$ Hz. Thus, we expect that, even with a network SNR threshold of $6.5\sqrt{2}$, our background rates will be approximated well below FARs of

$\lesssim 10^{-7}$ Hz when using search statistics $\vec{x} = \{\text{BSN}, \text{BCI}\}$.

We emphasize two points. First, the choice of search statistics matters greatly in this justification. Any thresholds on SNR would have a significant effect on the distribution of Λ at low-FAR if BCI was the only LRT search statistic. There would be no information available to weigh against the low-SNR, high-BCI events that the SNR thresholding removes. Secondly, this justification only holds when making detection statements at FARs of $\lesssim 10^{-7}$ Hz. In order to make detection statements on populations of quieter events that made reside at FARs of $\gtrsim 10^{-7}$ Hz, it would be essential to keep a low SNR threshold to avoid removing these “quieter” detection candidates. As a final point, it should be noted that the choice of building our background with an SNR threshold of $6.5\sqrt{2}$ instead of $5.5\sqrt{2}$ or even lower was made so that we can analyze longer durations of timeslided data in a computationally-feasible way, allowing us to make low-FAR detection statements.

C. LRT Results

In order to map a set of search statistics into a detection significance statement, we need to evaluate a signal-versus-noise LRT for both a set of foreground and a set of background event triggers. The foreground we used for our analysis consisted of the 0-lag triggers from the injection-filled data. The background consisted of the set of event triggers produced by our 2500 timeslides with a lower-network-SNR threshold of $6.5\sqrt{2}$. The final pieces needed for this LRT are likelihood models for our signal and noise hypotheses.

We trained our likelihoods using a Gaussian KDE optimized by the KL distance minimization criterion described in Appendix B. We trained our noise likelihoods using the events produced from the set of 100 timeslides with a lower network SNR threshold of $5.5\sqrt{2}$. At first glance, this training might appear to be misguided, since a large fraction of our training events (those with network SNRs between $5.5\sqrt{2}$ and $6.5\sqrt{2}$) cannot appear in our background. However, because the parameter space spanned by our background is a subset of the parameter space spanned by our training set, our training can still model the entire background parameter space. We trained our signal likelihoods on a set of astrophysically distributed SGs and WNBs, the exact populations of which will be described in § III C 3. A summary of this training, including the optimal KDE bandwidths for each training set, is presented in Table II. Examples of the resulting 1-D and 2-D likelihood distributions are shown in Figs. 7 and 8, respectively. The distributions of the different Bayes factors follow the general behavior we expect from them by construction: both BCI and BSN have more support at higher values for signals than for noise. This behavior is also seen when using SNR, which is not a Bayes factor, as a search statistic.

These distributions illustrate how information is

TABLE II. Descriptions of the signal and noise likelihood training sets and the relevant optimal bandwidths found for each.

Training Morphology	Training Statistics	Number of Events	BCI bandwidth	BSN bandwidth	oSNR bandwidth
Noise	BCI-BSN-oSNR	14311	1.22	1.46	0.21
Noise	BCI-BSN	14311	1.19	1.50	N/A
Noise	BCI	14311	0.75	N/A	N/A
SG and WNB	BCI-BSN-oSNR	895	1.65	6.00	0.61
SG and WNB	BCI-BSN	895	1.02	12.79	N/A
SG and WNB	BCI	895	1.32	N/A	N/A
SG	BCI-BSN-oSNR	639	1.54	6.36	0.66
SG	BCI-BSN	639	1.21	13.96	N/A
SG	BCI	639	1.36	N/A	N/A
WNB	BCI-BSN-oSNR	256	2.00	9.62	0.66
WNB	BCI-BSN	256	1.41	12.01	N/A
WNB	BCI	256	1.78	N/A	N/A

gained by using a combination of search statistics. For example, referencing the BCI-BSN plot in Fig. 8, we see that the outermost contour of the noise distribution is completely rejected by classifying any event with a BCI below 8 noise and anything else as a signal event. However, we can remove the same noise contour while retaining more of the signal distribution by classifying any event with a BCI below 8 *and* a BSN below 15 as noise and anything else as a signal event. Effectively, we constructed a more powerful decision surface. The LRT optimally constructs this decision surface, thus maximizing the probability of detecting a signal at a given false alarm probability. Furthermore, the amount of information contained within the search statistics defines how well the noise and signal distributions can be separated, which in turn determines how powerful the optimal decision surface is in terms of distinguishing signal from noise.

With these trained likelihoods in hand, we will now explore how the detection efficiency of our LRT changes as a function of: 1) the injected waveform morphologies, 2) the combination of search statistics used in the LRT, and 3) the signal populations used to train the signal likelihood.

1. Efficiency vs. Signal Morphology

Here we examine how oLIB’s detection efficiency changes as a function the GW waveform morphology. As noted, LIB uses sine-Gaussian templates when calculating the Bayes Factors, and thus we expect the oLIB pipeline to best recover sine-Gaussian signals. Fig. 9 shows the detection efficiency for several different injected morphologies as a function of the signal SNR residing within LIB’s frequency bandwidth. We note that, because Gaussian signals are centered at a frequency of zero, only a fraction of their total SNR is accessible to LIB. The shapes of the particular curves shown here are characteristic of the different morphologies in general. The efficiency curves for sine-Gaussians are logistic in shape, asymptoting at efficiencies of 1 at high SNRs.

The efficiency curves for Gaussian signals, which are sine-Gaussian signals in the limit $f_0 \rightarrow 0$ and $Q \rightarrow 0$, show the same logistic behavior at low-to-medium SNRs, but the efficiency degrades to 0 at high SNRs. Finally, the efficiency curves for white noise bursts appear to rise similarly at low SNRs, but the efficiency never reaches 1 and it again degrades to 0.

It may appear somewhat unintuitive that the efficiencies at the highest of SNRs are lower than the efficiencies at lower SNRs for Gaussian and white-noise burst signals. However, such behavior is understandable when considering the residuals of template mismatch. At low SNRs, the mismatch between the data stream and signal template is dominated by noise since the noise amplitude is comparable to the signal-template mismatch. As the SNR of the signal increases, the amplitude of the noise remains the same, but the amplitude of the signal-template mismatch residuals grows linearly with the signal amplitude. Thus, if a template cannot perfectly match the form of a GW signal, the signal-template mismatch will dominate the noise-template mismatch in the limit of high SNRs. In practice, these large residuals cause the BCIs to become extremely negative for high-SNR Gaussian and white-noise burst signals, which causes the LRT to label them as noise glitches despite having large BSN and SNR (it should be noted that although Gaussians are a subset of sine-Gaussians in the limit $f_0 \rightarrow 0$ and $Q \rightarrow 0$, our lower frequency prior bound of 64 Hz and lower Q prior bound of 2 prevent LIB from perfectly modeling Gaussians). While this behavior is unfortunate, since it could cause the oLIB pipeline to miss extremely loud (SNR $\gtrsim 100$) GW signals, we expect these types of signals to be extremely rare.

Table III shows the extensive results of our simulations. The results span three different LRTs, each using a detection threshold corresponding to a different FAR. For reference, the signal likelihood distribution for SNR in Fig. 7 provides a rough estimate of how often we expect to see signals at a given SNR. As is evident, we can expect a non-negligible amount of the detectable GW bursts to have network SNRs up to ~ 15 , which we will call “common” signals. Furthermore, while there will be

TABLE III. The SNRs at which the detection efficiency reached 10%, 50%, and 90% for different injected signal morphologies using LRTs corresponding to several different FARs. The LRTs were trained on both SG and WNB signals and were evaluated using BCI and BSN as search statistics. Detection efficiencies that were never reached at any SNR are denoted as N/A.

Morphology	FAR: 1 per decade (3×10^{-9} Hz)			FAR: 1 per year (3×10^{-8} Hz)			FAR: 1 per month (3×10^{-7} Hz)		
	SNR _{10%}	SNR _{50%}	SNR _{90%}	SNR _{10%}	SNR _{50%}	SNR _{90%}	SNR _{10%}	SNR _{50%}	SNR _{90%}
SG: $f_0 = 100$ Hz, $Q = 8.9$	14	33	220	13	17	36	9.7	14	21
SG: $f_0 = 153$ Hz, $Q = 8.9$	28	40	410	13	17	45	9.0	13	22
SG: $f_0 = 1053$ Hz, $Q = 9$	18	28	140	13	19	23	9.7	14	19
GA: $\tau = 0.1$ ms	16	30	N/A	14	19	43	11	17	25
GA: $\tau = 2.5$ ms	15	23	65	12	16	24	10	12	18
GA: $\tau = 4.0$ ms	16	21	71	12	16	24	11	13	17
WNB: $f_0 = 100$ Hz, $\Delta = 100$ Hz, $\tau = 100$ ms	54	N/A	N/A	25	N/A	N/A	17	33	N/A
WNB: $f_0 = 250$ Hz, $\Delta = 100$ Hz, $\tau = 100$ ms	50	N/A	N/A	24	N/A	N/A	17	29	N/A
WNB: $f_0 = 1000$ Hz, $\Delta = 10$ Hz, $\tau = 100$ ms	20	26	N/A	<19	24	34	<19	<19	24
WNB: $f_0 = 1000$ Hz, $\Delta = 1000$ Hz, $\tau = 10$ ms	32	N/A	N/A	24	44	N/A	22	34	N/A

detectable signals at an SNR of ~ 30 , these can be considered “rare” events. We will note that these distinctions of “common” and “rare” are only relative labels tied to the SNR distribution; they do not make quantitative predictions on the rate at which these GW signals events will be detected.

As the data shows, at a FAR significance of 1 per decade, we can expect oLIB to detect up to 10% of the “common” GW signals for the sine-Gaussian and Gaussian morphologies. We can also expect to detect “rare” loud events at about 10% efficiency for white noise bursts and at about 50% efficiency for sine-Gaussian and Gaussian signals. If we lower the significance of our detection threshold, we can detect these triggers at higher efficiencies across all morphologies, although it appears that we will be unable to detect the loudest white noise burst events at any FAR. However, we will stress again that the SNRs of white-noise bursts that we cannot detect are almost unrealistically large and that oLIB can be expected to detect non-negligible fractions of more reasonable high-SNR events (SNR ~ 30) across all morphologies.

2. Efficiency vs. LRT Parameters

We now explore how the detection efficiency varies as a function of the search statistics used as parameters in our LRT. As shown in Appendix A, likelihood ratios are sufficient statistics that optimally preserve the information contained within a set of search statistics about the binary signal-versus-noise hypothesis and adding another search statistic to the analysis can only increase the information. Thus, we would expect that if the likelihoods used in our LRT were accurate, an LRT with a greater number of search statistics would have a better-than-or-equal signal detection efficiency than an LRT utilizing fewer search statistics. We consider three different LRTs: one where the BCI is the only search statistic, one where both the BCI and BSN are used as search statistics, and one where BCI, BSN, and network Omicron

SNR (oSNR) are used as search statistics. We emphasize that the Bayes factors are natural search statistics to consider since they can be shown to be sufficient statistics when their hypotheses accurately model the possible data realizations, and that although oSNR is not generally a sufficient statistic, it still can only add information concerning the binary hypothesis to the vector of search statistics.

Table IV characterizes the detection efficiency for each of these LRTs. As expected, the BCI-BSN LRT generally outperforms the BCI-only LRT. There are a few instances where the BCI-only likelihood ratio test outperforms the BCI-BSN LRT, but we have to remember that we trained our LRT on a background set with a lower network SNR threshold of $5.5\sqrt{2}$ but are evaluating our LRT using a background with a lower network SNR threshold of $6.5\sqrt{2}$. As justified in § III B, this difference in thresholds should not affect our estimation of the rate of high- Λ events for a BCI-BSN LRT. However, this difference in thresholds causes us to underestimate the rate of high- Λ events when using a BCI-only LRT. That the BCI-BSN LRT tends to outperform the BCI-only LRT in spite of this underestimation of background rates in the high- Λ regime speaks to the power of the increased information resulting from the addition of search statistics. If we evaluated our LRTs using backgrounds with network SNR thresholds of $5.5\sqrt{2}$, we would expect the difference to be even greater.

However, the prediction that adding search statistics increases the detection efficiency appears to be negated when examining the BCI-BSN-oSNR LRT, which almost generally performs worse than the BCI-BSN LRT in signal detection efficiency. To be sure, the decrease in detection efficiency does not imply that there is actually less information available in the BCI-BSN-oSNR search statistic vector than in the BCI-BSN vector; we have proved that this cannot be the case. Instead, the addition of oSNR into the search statistic vector makes it more difficult to extract information about the signal-versus-noise hypothesis because the likelihood tails are harder to accurately model in three dimensions than in

TABLE IV. The SNRs at which the detection efficiency reached 10%, 50%, and 90% for different injected signal morphologies using LRTs evaluated with several different vectors of search statistics. The LRTs were trained on both SG and WNB signals and corresponded to an FAR of 1 per year. Detection efficiencies that were never reached at any SNR are denoted as N/A.

Morphology	BCI			BCI-BSN			BCI-BSN-oSNR		
	SNR _{10%}	SNR _{50%}	SNR _{90%}	SNR _{10%}	SNR _{50%}	SNR _{90%}	SNR _{10%}	SNR _{50%}	SNR _{90%}
SG: $f_0 = 100$ Hz, $Q = 8.9$	16	33	220	13	17	36	16	21	30
SG: $f_0 = 153$ Hz, $Q = 8.9$	28	40	410	13	17	45	15	22	38
SG: $f_0 = 1053$ Hz, $Q = 9$	14	26	140	13	19	23	17	20	24
GA: $\tau = 0.1$ ms	12	30	N/A	14	19	43	19	24	43
GA: $\tau = 2.5$ ms	14	23	65	12	16	24	14	20	25
GA: $\tau = 4.0$ ms	12	16	71	12	16	24	15	20	24
WNB: $f_0 = 100$ Hz, $\Delta = 100$ Hz, $\tau = 100$ ms	55	N/A	N/A	25	N/A	N/A	29	N/A	N/A
WNB: $f_0 = 250$ Hz, $\Delta = 100$ Hz, $\tau = 100$ ms	50	N/A	N/A	24	N/A	N/A	33	N/A	N/A
WNB: $f_0 = 1000$ Hz, $\Delta = 10$ Hz, $\tau = 100$ ms	<19	22	N/A	<19	24	34	27	49	N/A
WNB: $f_0 = 1000$ Hz, $\Delta = 1000$ Hz, $\tau = 10$ ms	23	N/A	N/A	24	44	N/A	28	46	N/A

two. Gaussian KDE tends to assign greater weight in sparsely-sampled regions of parameter space when using smaller training sets than when using larger training sets, since it has a less restrictive upper-limit on the event rate in these regions for the smaller training set. As a result, because our signal training sets were smaller than our noise training sets, these sparsely-sampled regions tend to be considered more signal-like than noise-like. This difference becomes more profound as the dimensionality of parameter space grows because the density of training points becomes even more diluted.

The most signal-like background event triggers we encounter tend to be loud, non-Gaussian noise events in each detector that become incoherently coincident in time once timeslides are applied. The BCI can label these triggers as noise since it assumes the detector contains non-Gaussian artifacts. However, loud non-Gaussian events can resemble signals more closely than Gaussian noise, and thus they can generate large values of BSN in addition to their large oSNR. If we trained on an infinite number of background triggers, we should encounter an infinite number of these events and be able to properly model the noise likelihood in this high-oSNR, high-BSN, low-BCI regime. However, since these outlier background triggers are quite rare, we may only encounter a few of them with finite training sets, meaning the sparsity argument described above becomes relevant. Thus, the lower density of training points in BCI-BSN-oSNR parameter space than in BCI-BSN parameter space can cause the significance of these outlier background events to be more inflated for the BCI-BSN-oSNR LRT than for the BCI-BSN LRT, explaining the degradation in detection efficiency. In conclusion, while adding search statistics should only increase detection efficiency if done properly, extracting this information becomes more difficult since the likelihoods become more difficult to model across all regimes. If our likelihood-fitting scheme were improved or more training points were considered, we would expect the BCI-BSN-oSNR LRT to be the most efficient LRT.

3. Efficiency vs. Training Population

Finally, we will explore how the signal population with which we train our signal likelihood affects our detection efficiency. We created three separate training populations: one consisting of only sine-Gaussians, one consisting of only white-noise bursts, and one consisting of both sine-Gaussians and white-noise bursts. We train the noise on the same population of events in all three scenarios, specifically, the set of timeslide events with a lower-network-SNR cutoff of $5.5\sqrt{2}$. The population of sine-Gaussians were distributed uniformly in spatial volume, uniformly in central frequency between 40 Hz and 1500 Hz, and uniformly in Q between 3 and 30. The population of white noise bursts were distributed uniformly in spatial volume, uniformly in starting frequency between 40 Hz and 1500 Hz, uniformly in bandwidth between 10 Hz and 1500 Hz, and uniformly in duration between 5 ms and 100 ms. The goal of these populations was to create an inclusive, realistic set of events to train on.

The detection efficiency results for all of these training scenarios are given in Table V, and the detection efficiencies are essentially identical across all training scenarios when the significance is thresholded at a FAR of 1 per year. To be sure, there is slightly more variation at a FAR significance of 1 per month (not shown). Although these deviations are probably statistically insignificant, the sine-Gaussian-trained LRT is slightly ($\mathcal{O}(1 \text{ SNR})$) more efficient at detecting some of the sine-Gaussian, Gaussian, and white noise burst morphologies, and the white-noise-burst-trained LRT is slightly ($\mathcal{O}(1 \text{ SNR})$) more efficient at detecting some of the other white noise burst morphologies. The fact that only slight variation in detection efficiency is seen at high FARs and that little-to-no variation is seen at low FARs suggests that the exact choice of training population has little effect on signal detection.

This feature is not surprising since the Gaussian KDE models the likelihoods well in regions of parameter space where the sample density is high, i.e., for the bulk of

TABLE V. The SNRs at which the detection efficiency reached 10%, 50%, and 90% for different injected signal morphologies using LRTs trained on several different signal populations. The LRTs were evaluated using BCI and BSN as search statistics and corresponded to an FAR of 1 per year. Detection efficiencies that were never reached at any SNR are denoted as N/A.

Morphology	SG and WNB			SG			WNB		
	SNR _{10%}	SNR _{50%}	SNR _{90%}	SNR _{10%}	SNR _{50%}	SNR _{90%}	SNR _{10%}	SNR _{50%}	SNR _{90%}
SG: $f_0 = 100$ Hz, $Q = 8.9$	13.(03)	17.(47)	36.(35)	13.(03)	17.(47)	36.(35)	13.(03)	17.(47)	36.(35)
SG: $f_0 = 153$ Hz, $Q = 8.9$	13.(04)	17.(49)	44.(68)	13.(04)	17.(49)	44.(68)	13.(04)	17.(49)	44.(68)
SG: $f_0 = 1053$ Hz, $Q = 9$	13.(05)	19.(02)	23.(02)	12.(71)	18.(54)	22.(98)	13.(05)	19.(02)	23.(02)
GA: $\tau = 0.1$ ms	13.(80)	19.(44)	43.(31)	13.(80)	19.(44)	43.(31)	13.(90)	20.(34)	43.(31)
GA: $\tau = 2.5$ ms	12.(14)	16.(23)	24.(35)	12.(14)	16.(23)	24.(35)	12.(14)	16.(23)	24.(35)
GA: $\tau = 4.0$ ms	12.(29)	15.(83)	23.(68)	12.(29)	15.(83)	23.(68)	12.(29)	15.(83)	23.(68)
WNB: $f_0 = 100$ Hz, $\Delta = 100$ Hz, $\tau = 100$ ms	25.(37)	N/A	N/A	25.(37)	N/A	N/A	25.(56)	N/A	N/A
WNB: $f_0 = 250$ Hz, $\Delta = 100$ Hz, $\tau = 100$ ms	24.(43)	N/A	N/A	24.(43)	N/A	N/A	24.(43)	N/A	N/A
WNB: $f_0 = 1000$ Hz, $\Delta = 10$ Hz, $\tau = 100$ ms	<19	24.(06)	34.(45)	<19	24.(06)	34.(45)	<19	24.(06)	34.(45)
WNB: $f_0 = 1000$ Hz, $\Delta = 1000$ Hz, $\tau = 10$ ms	23.(76)	43.(70)	N/A	23.(76)	44.(24)	N/A	23.(76)	43.(70)	N/A

the distribution. The bulk of the distribution is able to establish the general properties of “common” signal triggers as opposed to those of “common” noise events. Signal triggers tend to be louder than noise triggers (i.e., they have larger oSNR and BSN), and signal triggers tend to be more coherent than noise triggers (i.e., they have larger BCI). As seen in § III C 1, the differences in oLIB’s behavior for different morphologies only becomes pronounced at extremely-loud SNRs. These extremely-loud-SNR events are sufficiently rare that their contribution to the training is negligible when compared to that of the “common” bulk of events. Thus, because oLIB behaves similarly across morphologies for the “common” bulk of triggers that dominate training, the likelihood models are effectively invariant to the exact morphologies used in the training. That the likelihood training and in turn the LRT detection efficiency of the oLIB pipeline are both more-or-less invariant to exact signal population used in the training is a very convenient feature; it minimizes the impact of the pipeline’s largest source of arbitrariness.

IV. CONCLUSIONS

In this paper, we introduced the justification and methodology for a new end-to-end detection pipeline for GW bursts called oLIB. “End-to-end” means that this pipeline takes in calibrated strain data and compresses it into a set of search statistics that can be used to make a detection statement. Specifically, the compression involves several steps. First, the pipeline uses Omicron to flag stretches of calibrated strain data streams containing excess power as triggers. For computational reasons, these triggers are down-selected to the most “signal-like” subset by incoherently imposing constraints such as trigger clustering, vetoing based on data quality, and requiring time-of-flight time coincidence across the network of detectors. Once this incoherent down-selection is complete, these triggers are compressed into a set of search statistics with LIB, an MCMC algorithm used to cal-

culate Bayesian evidences that can then be used to form Bayes factors. Because Bayes factors are sufficient statistics for binary hypothesis testing, we expect the information lost concerning the signal-versus-noise hypothesis to be minimal as long as the set of hypotheses model the actual data realizations sufficiently well. In its standard configuration, the set of Bayes factors produced by LIB model three separate hypotheses: 1.) coherent sine-Gaussian signals in Gaussian noise, 2.) incoherent sine-Gaussian noise artifacts in Gaussian noise, and 3.) only Gaussian noise. We further compress this vector of search statistics into a scalar likelihood ratio, which preserve all of the information regarding the signal-versus-noise hypothesis contained within these search statistics. Finally, we use a likelihood-ratio test to rank events according to their signal-like significance. This LRT allows us to optimally extract this signal-versus-noise information that we have been preserving in our compression and make a detection statement via a false-alarm rate.

In order to demonstrate the pipeline’s validity, we ran it over a stretch of real interferometer data taken from the initial LIGO S6 science run. We also injected simulated GW signals into this data in order to study the pipeline’s behavior when analyzing detection candidates of varying morphology and strength. We showed that the incoherent down-selection of the Omicron-produced triggers was able to reduce the trigger rate by 4-5 orders of magnitude. We justified that the most signal-like background events will occur at high SNRs as long as the strength of the signals is represented within our set of search statistics in some fashion (namely by the inclusion of BSN or oSNR), allowing us to set a network SNR threshold without significantly underestimating the rate of high-significance background event triggers.

We showed that the the pipeline is capable of detecting events of network SNR ~ 15 at non-negligible efficiencies across a range of morphologies, though these efficiencies tend toward zero at very large SNRs for non-sine-Gaussian morphologies; template-mismatch residuals dominate the noise-mismatch residuals. We stress that observing events with such large SNRs would be

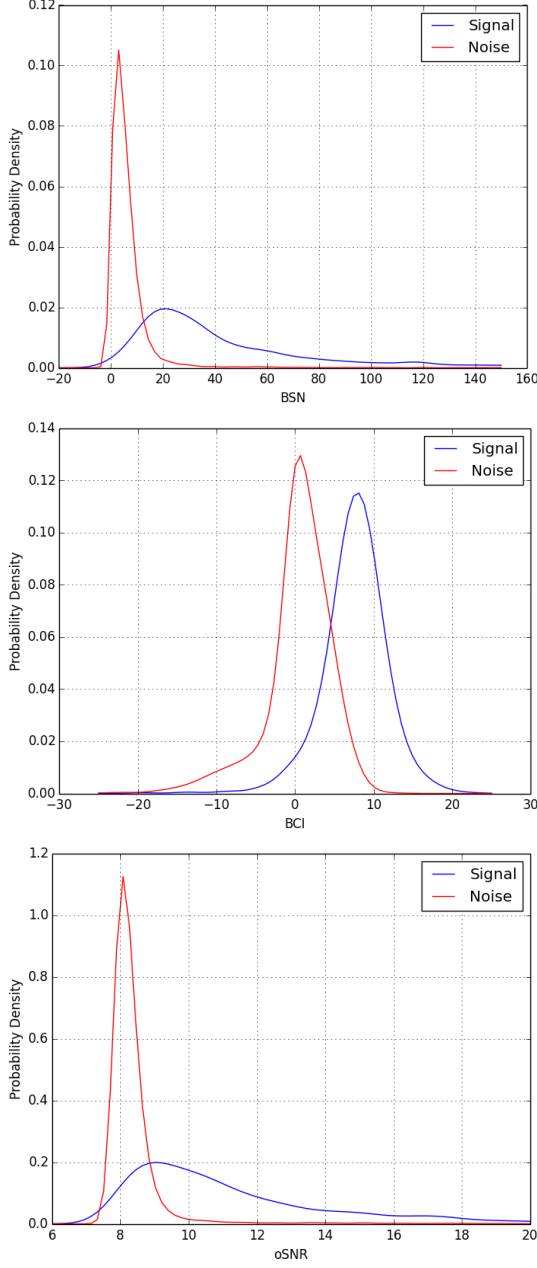


FIG. 7. The 1-dimensional likelihood marginals produced by optimally fitting the total 3-dimensional (BCI,BSN,oSNR) likelihood with Gaussian KDE and then marginalizing over two dimensions. The signal training population consisted of both sine-Gaussian and white-noise burst signals and the noise training population consisted of the background set with a lower-network-SNR threshold of $5.5\sqrt{2}$ (see Table II for training details). The likelihood ratio Λ is found by taking the ratio of the signal and noise likelihoods.

extremely rare in an astrophysically-distributed population of GW sources. We showed that, from a detection efficiency standpoint, the most powerful search involved an LRT that considered just the Bayes factors as search statistics and disregarded SNR. We attribute this fea-

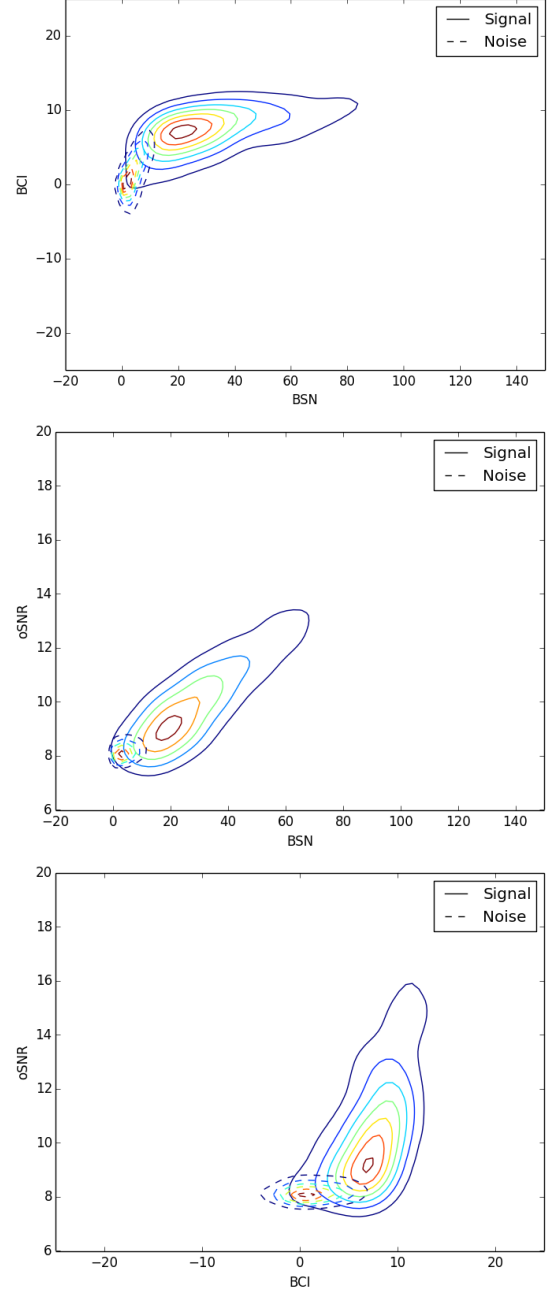


FIG. 8. The 2-dimensional likelihood marginals, produced in the same manner as in Fig. 7 but with the marginalization over one dimension.

ture to our likelihood models being more poorly modeled in their extreme tails in higher-dimensional parameter space. If more training points or improved likelihood modeling techniques were used to approximate these extreme tails, we expect the inclusion of SNR to only improve our detection efficiency. Finally, we showed that the detection efficiency of the LRT is quite robust against the exact choice of source population used when training the likelihoods.

The demonstration of oLIB's effectiveness and robust-

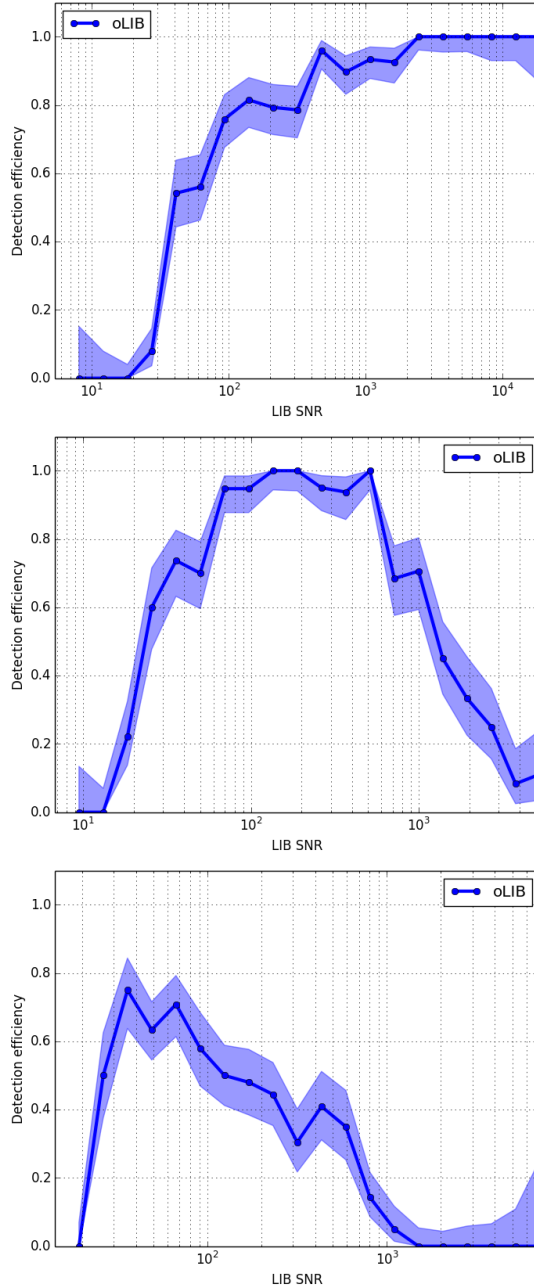


FIG. 9. The detection efficiency as a function of injected SNR (as estimated by LIB) at a FAR of 1 per decade for three different morphologies of injected waveforms: sine-Gaussian waveforms (top) with $f_0 = 153$ Hz and $Q = 8.9$, Gaussian waveforms (middle) with $\tau = 2.5$ ms, and white noise burst waveforms (bottom) with $f_0 = 1000$ Hz, $\Delta = 10$ Hz, and $\tau = 100$ ms. The LRT used here is trained on both sine-Gaussian and white noise bursts signal populations and is evaluated using BCI and BSN as search statistics. The 68% confidence region shown is derived from a binomial process with a uniform prior on the true detection efficiency.

ness is promising on several fronts. First, it provides a new end-to-end method for detecting GW bursts. At worst, oLIB provides overlap with existing methods that would be useful for consistency checks and validation, and, at best, oLIB provides increased sensitivity to areas of the burst parameter space. Quantifying this overlap with existing pipelines via comparison studies will be a priority moving forward. Finally, since the most efficient configuration of the oLIB pipeline involves combining several search statistics through an LRT to make a detection significance statement, we have successfully demonstrated a procedure that could be used to optimally combine the search statistics across several different pipelines into a joint detection significance statement.

V. ACKNOWLEDGMENTS

The authors acknowledge the support of the National Science Foundation, the LIGO Laboratory, and the Centre National de la Recherche Scientifique (CNRS). LIGO was constructed by the California Institute of Technology and Massachusetts Institute of Technology with funding from the National Science Foundation and operates under cooperative agreement PHY-0757058. The authors would like to acknowledge the LIGO Data Grid clusters, without which the simulations could not have been performed. Specifically, we thank the Albert Einstein Institute in Hannover, supported by the Max-Planck-Gesellschaft, for use of the Atlas high-performance computing cluster. We would like to thank Peter Couvares and Josh Willis for help with optimizing our code. We would also like to thank Lindy Blackburn, Kipp Cannon, Phillip Graff, Satya Mohapatra, Matt Pitkin, Laura Sampson, Ruslan Vaulin, Alberto Vecchio, John Veitch, and the LIGO-Virgo Burst search working group for useful comments and discussion. This is LIGO document number P1500220.

[1] T. L. S. Collaboration, Classical and Quantum Gravity **32**, 074001 (2015).

[2] F. A. et al, Classical and Quantum Gravity **32**, 024001 (2015).

- [3] C. Affeldt, K. Danzmann, K. L. Dooley, H. Grote, M. He-
witson, S. Hild, J. Hough, J. Leong, H. Lck, M. Pri-
jatelj, S. Rowan, A. Rdiger, R. Schilling, R. Schnabel,
E. Schreiber, B. Sorazu, K. A. Strain, H. Vahlbruch,
B. Willke, W. Winkler, and H. Wittel, *Classical and
Quantum Gravity* **31**, 224002 (2014).
- [4] J. Aasi *et al.* (VIRGO, LIGO Scientific), (2013),
arXiv:1304.0670 [gr-qc].
- [5] C. S. Unnikrishnan, *International Journal of Modern
Physics D* **22**, 1341010 (2013).
- [6] Y. Aso, Y. Michimura, K. Somiya, M. Ando,
O. Miyakawa, T. Sekiguchi, D. Tatsumi, and H. Yam-
amoto (The KAGRA Collaboration), *Phys. Rev. D* **88**,
043007 (2013).
- [7] J. A. et al, *Classical and Quantum Gravity* **27**, 173001
(2010).
- [8] C. D. Ott, A. Burrows, L. Dessart, and E. Livne, *Phys.
Rev. Lett.* **96**, 201102 (2006).
- [9] C. D. Ott, *Classical and Quantum Gravity* **26**, 063001
(2009).
- [10] A. Burrows, E. Livne, L. Dessart, C. D. Ott, and J. Murphy,
The Astrophysical Journal **640**, 878 (2006).
- [11] A. Burrows, L. Dessart, E. Livne, C. D. Ott, and J. Murphy,
The Astrophysical Journal **664**, 416 (2007).
- [12] H. Dimmelmeier, C. D. Ott, A. Marek, and H.-T. Janka,
Phys. Rev. D **78**, 064056 (2008).
- [13] S. Mohapatra, L. Cadonati, S. Caudill, J. Clark,
C. Hanna, S. Klimenko, C. Pankow, R. Vaulin, G. Vedovato,
and S. Vitale, *Phys. Rev. D* **90**, 022001 (2014),
arXiv:1405.6589 [gr-qc].
- [14] R. Essick, S. Vitale, E. Katsavounidis, G. Vedovato, and
S. Klimenko, *The Astrophysical Journal* **800**, 81 (2015).
- [15] J. Logue, C. D. Ott, I. S. Heng, P. Kalmus, and J. H. C.
Scargill, *Phys. Rev. D* **86**, 044023 (2012).
- [16] J. e. a. Abadie (The LIGO Scientific Collaboration and
The Virgo Collaboration), *Phys. Rev. D* **85**, 122007
(2012).
- [17] S. Klimenko, S. Mohanty, M. Rakhmanov, and G. Mit-
selmakher, *Phys. Rev. D* **72**, 122002 (2005), arXiv:gr-
qc/0508068.
- [18] S. Klimenko, I. Yakushin, A. Mercer, and G. Mit-
selmakher, *Classical and Quantum Gravity* **25**, 114029
(2008), arXiv:0802.3232.
- [19] S. Klimenko, G. Vedovato, M. Drago, G. Mazzolo,
G. Mitselmakher, C. Pankow, G. Prodi, V. Re, F. Salemi,
and I. Yakushin, *Phys. Rev. D* **83**, 102001 (2011),
arXiv:1101.5408.
- [20] P. J. Sutton, G. Jones, S. Chatterji, P. Kalmus, I. Leonor,
S. Poprocki, J. Rollins, A. Searle, L. Stein, M. Tinto, and
M. Was, *New Journal of Physics* **12**, 053034 (2010).
- [21] J. B. Kanner, T. B. Littenberg, N. Cornish, M. Millhouse,
E. Xhakaj, F. Salemi, M. Drago, G. Vedovato, and S. Kli-
menko, ArXiv e-prints (2015), arXiv:1509.06423 [astro-
ph.IM].
- [22] N. J. Cornish and T. B. Littenberg, *Classical and Quantum
Gravity* **32**, 135012 (2015).
- [23] T. B. Littenberg and N. J. Cornish, *Phys. Rev. D* **91**,
084034 (2015).
- [24] D. Gabor, *J. IEE* **93**, 429 (1946).
- [25] J. C. Brown, *J. Acoust. Soc. Am* **92**, 2698 (1992).
- [26] S. Chatterji, L. Blackburn, G. Martin, and E. Katsavounidis,
Classical and Quantum Gravity **21**, S1809
(2004).
- [27] J. Veitch and A. Vecchio, *Phys. Rev. D* **81**, 062003
(2010).
- [28] J. Veitch, V. Raymond, B. Farr, W. Farr, P. Graff,
S. Vitale, B. Aylott, K. Blackburn, N. Christensen,
M. Coughlin, W. Del Pozzo, F. Feroz, J. Gair, C.-
J. Haster, V. Kalogera, T. Littenberg, I. Mandel,
R. O’Shaughnessy, M. Pitkin, C. Rodriguez, C. Röver,
T. Sidery, R. Smith, M. Van Der Sluys, A. Vecchio,
W. Vousden, and L. Wade, *Phys. Rev. D* **91**, 042003
(2015).
- [29] J. A. et al., *Classical and Quantum Gravity* **32**, 115012
(2015).
- [30] J. Neyman and E. S. Pearson, *Philosophical Transactions
of the Royal Society of London A: Mathematical, Physi-
cal and Engineering Sciences* **231**, 289 (1933).
- [31] R. Essick, L. Blackburn, and E. Katsavounidis, *Classical
and Quantum Gravity* **30**, 155010 (2013).
- [32] J. R. Smith, T. Abbott, E. Hirose, N. Leroy, D. MacLeod,
J. McIver, P. Saulson, and P. Shawhan, *Classical and
Quantum Gravity* **28**, 235005 (2011).
- [33] J. Skilling, *Bayesian Anal.* **1**, 833 (2006).
- [34] K. Cannon, C. Hanna, and J. Peoples, ArXiv e-prints
(2015), arXiv:1504.04632 [astro-ph.IM].
- [35] J. e. a. Aasi ((LIGO Scientific Collaboration and Virgo
Collaboration)), *Phys. Rev. Lett.* **112**, 131101 (2014).
- [36] R. Biswas, P. R. Brady, J. Burguet-Castell, K. Can-
non, J. Clayton, A. Dietz, N. Fotopoulos, L. M. Goggia-
n, D. Keppel, C. Pankow, L. R. Price, and R. Vaulin, *Phys.
Rev. D* **85**, 122008 (2012), arXiv:1201.2959 [gr-qc].
- [37] M. Ws, M.-A. Bizouard, V. Brisson, F. Cavalier,
M. Davier, P. Hello, N. Leroy, F. Robinet, and
M. Vavouliidis, *Classical and Quantum Gravity* **27**,
015005 (2010).
- [38] Open web page, URL <http://www.ligo.org/science/GW100916/index.php>.

Appendix A: Optimality of the Likelihood Ratio Test

1. Neyman-Pearson Lemma

Here we provide a proof of the Neyman-Pearson Lemma [30], which states that the likelihood-ratio test maximizes the probability of detecting a signal P_D at a given false alarm probability P_F for binary hypothesis testing.

Binary hypothesis testing involves two hypotheses, a positive hypothesis H_1 (e.g., a GW signal present in the data) and a null hypothesis H_0 (e.g., no GW signal present in the data). Any binary hypothesis test should make a prediction on which hypothesis is correct based on an n -dimension vector of data parameters \vec{x} . Effectively, the test divides the entire parameter space \mathcal{X} (where $\vec{x} \in \mathcal{X} \forall \vec{x}$), into two non-overlapping subspaces \mathcal{X}_1 and \mathcal{X}_0 . If $\vec{x} \in \mathcal{X}_1$ the test predicts that H_1 is the correct hypothesis, and if $\vec{x} \in \mathcal{X}_0$ the test predicts that H_0 is the correct hypothesis. With these subspaces defined,

we can express P_D and P_F , respectively, as:

$$\begin{aligned} P_D &= \int_{\mathcal{X}_1} P_{x|H}(\vec{x}|H = H_1) d\vec{x} \\ &= 1 - \int_{\mathcal{X}_0} P_{x|H}(\vec{x}|H = H_1) d\vec{x} \end{aligned} \quad (\text{A1})$$

$$\begin{aligned} P_F &= \int_{\mathcal{X}_1} P_{x|H}(\vec{x}|H = H_0) d\vec{x} \\ &= 1 - \int_{\mathcal{X}_0} P_{x|H}(\vec{x}|H = H_0) d\vec{x} \end{aligned} \quad (\text{A2})$$

where we have used the fact that the integral of probability over all of \mathcal{X} must be 1. Thus, the detection probability P_D is the total probability that our binary hypothesis test predicts the positive hypothesis H_1 when the true hypothesis is in fact H_1 , and the false-alarm probability P_F is the total probability that our binary hypothesis predicts H_1 when the true hypothesis is actually the null hypothesis H_0 .

We now wish to maximize P_D while constraining P_F to a given value β . This maximization can be accomplished through the use of a Lagrange multiplier α , and our optimization problem can be expressed as the minimization of Ψ with respect to our decision subspaces \mathcal{X}_0 and \mathcal{X}_1 where we define Ψ as

$$\Psi = (1 - P_D) + \alpha(P_F - \beta). \quad (\text{A3})$$

Using Eq. A1 and Eq. A2, we can rewrite Eq. A3 as

$$\begin{aligned} \Psi &= \alpha(1 - \beta) + \\ &\int_{\mathcal{X}_0} [P_{x|H}(\vec{x}|H = H_1) - \alpha P_{x|H}(\vec{x}|H = H_0)] d\vec{x}. \end{aligned} \quad (\text{A4})$$

Our aim is to choose our decision subspaces such that we minimize Ψ . From Eq. A4, it is clear that we can do so by choosing to include only negative integrands in the integral, i.e., we only integrate of regions of \mathcal{X} where $P_{x|H}(\vec{x}|H = H_1) \leq \alpha P_{x|H}(\vec{x}|H = H_0)$. This optimal division of \mathcal{X} into \mathcal{X}_0 and \mathcal{X}_1 can be equivalently expressed as

$$\frac{P_{x|H}(\vec{x}|H = H_1)}{P_{x|H}(\vec{x}|H = H_0)} \stackrel{\hat{H}=H_1}{\underset{\hat{H}=H_0}{\gtrless}} \alpha \quad (\text{A5})$$

which is just the LRT as defined in Eq. 8. Thus, the likelihood-ratio test is the binary hypothesis test that chooses the decision surface in \mathcal{X} such that P_D is maximized at a given P_F .

Finally, we can argue that the Neyman-Person lemma implies that both the false-alarm probability P_F and the detection probability P_D are monotonically decreasing functions of the likelihood-ratio threshold α . Suppose we have two thresholds α_a and α_b with $\alpha_a > \alpha_b$. This implies that the null region of parameter space \mathcal{X}_0

is larger for threshold α_a than for threshold α_b , i.e., $|\mathcal{X}_{0,a}| \geq |\mathcal{X}_{0,b}|$. Using the non-negativity of probability distributions, Eqs. A1 and A2 directly imply that both $P_{D,a} \leq P_{D,b}$ and $P_{F,a} \leq P_{F,b}$ for any arbitrary thresholds $\alpha_a > \alpha_b$. Thus, both P_D and P_F are monotonically decreasing functions of the Neyman-Pearson likelihood-ratio threshold.

2. Likelihood Ratio as a Sufficient Statistic for Binary Hypothesis Testing

a. Definition of a Sufficient Statistic and the Data Processing Inequality

In addition to the optimality of the LRT as outlined by the Neyman-Pearson Lemma, we can show that the likelihood ratio is optimal in the sense that it is a sufficient statistic for binary hypothesis testing. A statistic $t(\vec{x})$ is any function (vector or scalar) that processes a data vector \vec{x} . A statistic $t(\vec{x})$ is said to be sufficient with respect to $P_{x,H}(\vec{x}, H)$ if and only if

$$P_{x|t,H}(\vec{x}|t(\vec{x}), H) = P_{x|t}(\vec{x}|t(\vec{x})) \quad (\text{A6})$$

where \vec{x} and H are general random variables whose symbols we choose to make our application to binary hypothesis testing easier. We can use this definition to derive a more illustrative definition of sufficiency: a statistic $t(\vec{x})$ is said to be sufficient with respect to $P_{x,H}(\vec{x}, H)$ if and only if

$$P_{H|x}(H|\vec{x}) = P_{H|t}(H|t(\vec{x})) \quad (\text{A7})$$

The proof is as follows:

- Assuming $P_{H|x}(H|\vec{x}) = P_{H|t}(H|t(\vec{x}))$: We can write the distribution $P_{x|t,H}(\vec{x}|t(\vec{x}), H)$ as

$$\begin{aligned} P_{x|t,H}(\vec{x}|t(\vec{x}), H) &= \frac{P_{x,t,H}(\vec{x}, t(\vec{x}), H)}{P_{t,H}(t(\vec{x}), H)} \\ &= \frac{P_{H|t,x}(H|t(\vec{x}), \vec{x}) P_{x|t}(\vec{x}|t(\vec{x})) P_t(t(\vec{x}))}{P_{H|t}(H|t(\vec{x})) P_t(t(\vec{x}))} \end{aligned} \quad (\text{A8})$$

and cancel the $P_t(t(\vec{x}))$ terms. Then we note that the first term in the numerator is equal to $P_{H|x}(H|\vec{x})$ because \vec{x} completely determines $t(\vec{x})$ and that the denominator is equal to $P_{H|x}(H|\vec{x})$ by our above assumption. Canceling these terms gives $P_{x|t,H}(\vec{x}|t(\vec{x}), H) = P_{x|t}(\vec{x}|t(\vec{x}))$, which is the definition of a sufficient statistic given by Eq. A6.

- Assuming $t(\vec{x})$ is a sufficient statistic: Because \vec{x}

completely determines $t(\vec{x})$, we can write

$$\begin{aligned} P_{H|x}(H|\vec{x}) &= P_{H|x,t}(H|\vec{x}, t(\vec{x})) \\ &= \frac{P_{H,x,t}(H, \vec{x}, t(\vec{x}))}{P_{x,t}(\vec{x}, t(\vec{x}))} \\ &= \frac{P_{x|t,H}(\vec{x}|t(\vec{x}), H)P_{H|t}(H|t(\vec{x}))P_t(t(\vec{x}))}{P_{x|t}(\vec{x}|t(\vec{x}))P_t(t(\vec{x}))} \end{aligned} \quad (\text{A9})$$

and cancel the $P_t(t(\vec{x}))$ terms. We then use the definition of a sufficient statistic, given by Eq. A6, to cancel the first term in the numerator with the denominator to give $P_{H|x}(H|\vec{x}) = P_{H|t}(H|t(\vec{x}))$, thus completing the proof.

Eq. A7 is illustrative because it states that equivalent inference of H can be done with knowledge of $t(\vec{x})$ as with knowledge of \vec{x} . In effect, a statistic is sufficient if it preserves all of the information shared by two random variables H and \vec{x} .

We can rigorously quantify this idea of information. The mutual information contained between two random variables can be defined as

$$I(a; b) = \mathcal{H}(a) - \mathcal{H}(a|b) = \mathcal{H}(b) - \mathcal{H}(b|a) \quad (\text{A10})$$

where $\mathcal{H}(\cdot)$ and $\mathcal{H}(\cdot| \cdot)$ are the entropy and conditional entropy, respectively, defined by:

$$\mathcal{H}(a) = - \sum_{a'} P_a(a') \log P_a(a') \quad (\text{A11})$$

$$\mathcal{H}(a|b) = - \sum_{a', b'} P_{a,b}(a', b') \log P_{a|b}(a'|b'). \quad (\text{A12})$$

Because the entropy of a distribution is a measure of its distributional uncertainty, the mutual information of two random variables measures how the knowledge of one of the variables reduces the uncertainty of the other. A straightforward application of Gibb's inequality can be

used to show that $\mathcal{H}(a|b) \leq \mathcal{H}(a)$, meaning $I(a; b) \geq 0$. We can also use the explicit definitions of the entropies to show that

$$I(a; b) = \sum_{a', b'} P_{a,b}(a', b') \log \frac{P_{a,b}(a', b')}{P_a(a')P_b(b')} \quad (\text{A13})$$

With these definitions in place, we can prove the Data Processing Inequality (DPI), which holds in general for any statistic $t(\vec{x})$. Using the same notation as above, where \vec{x} is a data vector, $t(\vec{x})$ is a statistic, and H is a general random variable, we can write

$$I(H; \vec{x}, t(\vec{x})) = \mathcal{H}(H) - \mathcal{H}(H|\vec{x}, t(\vec{x})) \quad (\text{A14})$$

$$\begin{aligned} \mathcal{H}(H) - \mathcal{H}(H|\vec{x}) + \mathcal{H}(H|\vec{x}) - \mathcal{H}(H|\vec{x}, t(\vec{x})) &= \\ \mathcal{H}(H) - \mathcal{H}(H|t(\vec{x})) + \mathcal{H}(H|t(\vec{x})) - \mathcal{H}(H|\vec{x}, t(\vec{x})) \end{aligned} \quad (\text{A15})$$

$$I(H; \vec{x}) + I(H; t(\vec{x})|\vec{x}) = I(H; t(\vec{x})) + I(H; \vec{x}|t(\vec{x})) \quad (\text{A16})$$

By explicitly writing out the form of $I(H; t(\vec{x})|\vec{x})$, we find

$$\begin{aligned} I(H; t(\vec{x})|\vec{x}) &= \sum_{H,t} P_{H,t|x}(H, t(\vec{x})|\vec{x}) \log \frac{P_{t|H,x}(t(\vec{x})|H, \vec{x})P_{H|x}(H|\vec{x})}{P_{t|x}(t(\vec{x})|\vec{x})P_{H|x}(H|\vec{x})} \\ &= 0 \end{aligned} \quad (\text{A17})$$

where the second equality can be seen by noticing that $P_{t|H,x}(t(\vec{x})|H, \vec{x}) = P_{t|x}(t(\vec{x})|\vec{x}) = 1$ because \vec{x} determines $t(\vec{x})$ exactly, meaning the log term goes to zero.

Since $I(H; \vec{x}|t(\vec{x})) \geq 0$, we have proved in general the DPI:

$$I(H; \vec{x}) \geq I(H; t(\vec{x})). \quad (\text{A18})$$

The DPI states that any processing of a random data vector \vec{x} into a statistic $t(\vec{x})$ can only preserve or degrade the amount of information available regarding the random variable H . As it turns out, the equality holds precisely when the statistic $t(\vec{x})$ is sufficient. We can see this by writing out $I(H; \vec{x}|t(\vec{x}))$ explicitly in the form

$$I(H; \vec{x}|t(\vec{x})) = \sum_{H,x} P_{H,x|t}(H, \vec{x}|t(\vec{x})) \log \frac{P_{x|H,t}(\vec{x}|H, t(\vec{x}))P_{H|t}(H|t(\vec{x}))}{P_{x|t}(\vec{x}|t(\vec{x}))P_{H|t}(H|t(\vec{x}))} \quad (\text{A19})$$

and noticing that it goes to zero if $P_{x|H,t}(\vec{x}|H, t(\vec{x})) = P_{x|t}(\vec{x}|t(\vec{x}))$, i.e., the conditions for a sufficient statistic given by Eq. A6. Thus, if a statistic $t(\vec{x})$ is sufficient with respect to the joint probability distribution $P_{x,H}(\vec{x}, H)$ of a random data vector \vec{x} and another random variable H , then the statistic contains the same amount of information regarding H as the data itself.

b. Neyman-Fisher Factorization

In order to prove that the likelihood ratio is a sufficient statistic, it is useful to first prove two different theorems regarding sufficient statistics. The first theorem is that a statistic $t(\vec{x})$ is sufficient with respect to $P_{x,H}(\vec{x}, H)$ if and only if $P_{x|H,t}(\vec{x}|H, t(\vec{x}))$ is independent of the variable H . The proof is straightforward:

1. Assuming $P_{x|H,t}(\vec{x}|H, t(\vec{x}))$ is independent of the variable H : We can write the distribution $P_{x|t}(\vec{x}|t(\vec{x}))$ as a marginalization over H , namely:

$$\begin{aligned} P_{x|t}(\vec{x}|t(\vec{x})) &= \sum_H P_{x|H,t}(\vec{x}|H, t(\vec{x})) P_{H|t}(H|t(\vec{x})) \\ &= P_{x|H,t}(\vec{x}|H, t(\vec{x})) \sum_H P_{H|t}(H|t(\vec{x})) \quad (\text{A20}) \\ &= P_{x|H,t}(\vec{x}|H, t(\vec{x})) \end{aligned}$$

thus satisfying the condition Eq. A6 for $t(\vec{x})$ being a sufficient statistic.

2. Assuming $t(\vec{x})$ is a sufficient statistic: We can start from the condition for $t(\vec{x})$ being a sufficient statistic

$$P_{x|H,t}(\vec{x}|H, t(\vec{x})) = P_{x|t}(\vec{x}|t(\vec{x})) = f(\vec{x}) \quad (\text{A21})$$

and directly see that $P_{x|H,t}(\vec{x}|H, t(\vec{x}))$ is a function of \vec{x} alone and is thus independent of the variable H .

Using this theorem, we can prove the Neyman-Fisher factorization theorem. This powerful theorem states that a statistic $t(\vec{x})$ is sufficient with respect to $P_{x,H}(\vec{x}, H)$ if and only if $P_{x|H}(\vec{x}|H)$ can be factored into the form $P_{x|H}(\vec{x}|H) = a(t(\vec{x}), H)b(\vec{x})$ for some functions a and b . The proof is as follows:

1. Assuming $P_{x|H}(\vec{x}|H) = a(t(\vec{x}), H)b(\vec{x})$: We first use Bayes' theorem to write $P_{x|H,t}(\vec{x}|H, t(\vec{x}))$ as

$$\begin{aligned} P_{x|H,t}(\vec{x}|H, t(\vec{x})) &= \frac{P_{t|x,H}(t(\vec{x})|\vec{x}, H)P_{x|H}(\vec{x}|H)}{P_{t|H}(t(\vec{x})|H)} \\ &= \frac{P_{t|x,H}(t(\vec{x})|\vec{x}, H)P_{x|H}(\vec{x}|H)}{\sum_{x'} P_{x,t|H}(\vec{x}', t(\vec{x})|H)}. \quad (\text{A22}) \end{aligned}$$

We can simplify this expression by noting that $P_{t|x,H}(t(\vec{x})|\vec{x}, H) = 1$ and $P_{x,t|H}(\vec{x}', t(\vec{x})|H) = P_{x|H}(\vec{x}'|H)\delta_{t(\vec{x}), t(\vec{x}')}}$ since \vec{x} completely determines $t(\vec{x})$. Substituting in the Neyman-Fisher factorization, we then have

$$\begin{aligned} P_{x|H,t}(\vec{x}|H, t(\vec{x})) &= \frac{a(t(\vec{x}), H)b(\vec{x})}{\sum_{x':t(\vec{x}')=t(\vec{x})} a(t(\vec{x}'), H)b(\vec{x}')} \\ &= \frac{b(\vec{x})}{\sum_{x':t(\vec{x}')=t(\vec{x})} b(\vec{x}')} \\ &= f(\vec{x}) \quad (\text{A23}) \end{aligned}$$

where we were able to factor $a(t(\vec{x}), H)$ out of the sum due to the imposed constraint $t(\vec{x}') = t(\vec{x})$. Thus, we see that $P_{x|H,t}(\vec{x}|H, t(\vec{x}))$ is independent of H , meaning $t(\vec{x})$ is a sufficient statistic.

2. Assuming $t(\vec{x})$ is a sufficient statistic: We use the fact that \vec{x} completely determines $t(\vec{x})$ to write

$$\begin{aligned} P_{x|H}(\vec{x}|H) &= P_{x,t|H}(\vec{x}, t(\vec{x})|H) \\ &= P_{x|t,H}(\vec{x}|t(\vec{x}), H)P_{t|H}(t(\vec{x})|H) \quad (\text{A24}) \end{aligned}$$

and then use the condition for a sufficient statistic Eq. A6 to write

$$\begin{aligned} P_{x|H}(\vec{x}|H) &= P_{x|t}(\vec{x}|t(\vec{x}))P_{t|H}(t(\vec{x})|H) \\ &= a(t(\vec{x}), H)b(\vec{x}) \end{aligned} \quad (\text{A25})$$

where $a(t(\vec{x}), H) = P_{t|H}(t(\vec{x})|H)$ and $b(\vec{x}) = P_{x|t}(\vec{x}|t(\vec{x}))$. This result is our desired factorization.

c. Proof that Likelihood Ratios are Sufficient Statistics for Hypothesis Testing

Using the proofs above, we can finally show that the likelihood ratio $\Lambda(\vec{x})$ is a sufficient statistic with respect to $P_{x,H}(\vec{x}, H)$ where \vec{x} is a random vector of analysis statistics and $H \in \{H_0, H_1\}$ is a random hypothesis variable for binary hypothesis testing. In order to prove this statement, we consider the form of $P_{x|H}(\vec{x}|H)$ under both hypotheses:

$$P_{x|H}(\vec{x}|H = H_1) = \Lambda(\vec{x}) \cdot P_{x|H}(\vec{x}|H = H_0) \quad (\text{A26})$$

$$P_{x|H}(\vec{x}|H = H_0) = 1 \cdot P_{x|H}(\vec{x}|H = H_0) \quad (\text{A27})$$

where $\Lambda(\vec{x}) \equiv \frac{P_{x|H}(\vec{x}|H = H_1)}{P_{x|H}(\vec{x}|H = H_0)}$ is the likelihood ratio. Thus, by defining $\Lambda_{i,j}(\vec{x}) \equiv \frac{P_{x|H}(\vec{x}|H = H_i)}{P_{x|H}(\vec{x}|H = H_j)}$, $a(\Lambda(\vec{x}), H_i) = \Lambda_{i,0}(\vec{x})$, and $b(\vec{x}) = P_{x|H}(\vec{x}|H = H_0)$, we can complete the Neyman-Fisher factorization, proving that $\Lambda(\vec{x})$ is a sufficient statistic for binary hypothesis testing.

It is straightforward to generalize this proof from binary hypothesis testing to N -dimensional hypothesis testing where $N \geq 2$. Here, let our statistic be $\vec{\Lambda}(\vec{x})$, the set of all possible likelihood ratios among the N hypotheses $\vec{H} = \{H_0, H_1, \dots, H_N\}$. More formally, $\vec{\Lambda}(\vec{x}) = \{\dots, \Lambda_{i,j}(\vec{x}), \dots\}$ for all $i, j \in \{0, 1, \dots, N\}$. We can then write down the form for $P_{x|H}(\vec{x}|H)$ for any arbitrary hypothesis H_i :

$$P_{x|H}(\vec{x}|H = H_i) = \Lambda_{i,0}(\vec{x}) \cdot P_{x|H}(\vec{x}|H = H_0). \quad (\text{A28})$$

Thus, by defining $a(\vec{\Lambda}(\vec{x}), H) = \Lambda_{i,0}(\vec{x})$ and $b(\vec{x}) = P_{x|H}(\vec{x}|H = H_0)$, we see that we can complete the Neyman-Fisher factorization, proving that the set of all likelihood ratios $\vec{\Lambda}(\vec{x})$ is a sufficient statistic for N -dimensional hypothesis testing. Actually, closer inspection shows that we do not even need $\vec{\Lambda}(\vec{x})$ to be the full set of likelihood ratios between all hypotheses, but rather only the set of likelihood ratios between all individual hypotheses and a particular hypothesis H_0 (since the likelihood ratio of any two arbitrary hypotheses H_i and H_j can be computed through the ratio $\Lambda_{i,j}(\vec{x}) = \frac{\Lambda_{i,0}(\vec{x})}{\Lambda_{j,0}(\vec{x})}$).

This property implies that the set of likelihood ratios spanning all possible hypotheses $\vec{\Lambda}(\vec{x})$ is optimal in a data processing sense. As we proved in Appendix A 2 a, a

statistic that is sufficient with respect to a random data vector \vec{x} and a random variable H preserves all of the mutual information shared between those two variables. Thus, in N -dimensional hypothesis testing, no information about the actual hypothesis H is lost when compressing the statistic vector \vec{x} into the set of likelihood ratios $\vec{\Lambda}(\vec{x})$. While other combinations of \vec{x} may also be sufficient statistics (sufficient statistics are not inherently unique), they cannot contain more information about H than $\vec{\Lambda}(\vec{x})$ does, and thus $\vec{\Lambda}(\vec{x})$ is an optimal statistic in N -dimensional hypothesis testing.

On a final note, let us consider the case where all of the specific hypotheses H in the N -dimensional \vec{H} can be categorized as an element of a greater positive-versus-null binary hypothesis H_{bin} , so that $H \in H_{\text{bin}} \in \{H_{\text{null}}, H_{\text{pos}}\}$ (e.g., if \vec{H} contains different signal and noise models, but all are sub-models of the greater signal or noise hypotheses H_{signal} and H_{noise}). In this scenario, assuming that the true hypothesis is an element of \vec{H} , the original data vector \vec{x} can be compressed into the set of likelihood ratios spanning all possible hypotheses $\vec{\Lambda}(\vec{x})$, and this compression is lossless with respect to the information concerning the specific hypothesis H . We can show that this compression is also lossless with respect to the information concerning the binary hypothesis H_{bin} by considering the likelihoods for both the null and positive binary hypotheses:

$$\begin{aligned} P_{x|H_{\text{bin}}}(\vec{x}|H_{\text{null}}) &= \sum_i P_{x|H, H_{\text{bin}}}(\vec{x}|H_i, H_{\text{null}}) P_{H|H_{\text{bin}}}(H_i|H_{\text{null}}) \\ &= P_{x|H, H_{\text{bin}}}(\vec{x}|H_0, H_{\text{null}}) \\ &\quad \cdot \sum_{H_i \in H_{\text{null}}} \Lambda_{i,0}(\vec{x}) P_{H|H_{\text{bin}}}(H_i|H_{\text{null}}) \end{aligned} \quad (\text{A29})$$

$$I(H; \vec{x}, x_+) = \sum_{H, x, x_+} P_{H,x}(H, \vec{x}, x_+) \log \frac{P_{H,x}(H, \vec{x}, x_+)}{P_x(\vec{x}, x_+) P_H(H)} \quad (\text{A31})$$

$$I(H; \vec{x}, x_+) = \sum_{H, x, x_+} P_{H,x}(H, \vec{x}, x_+) \log \frac{P_{H,x}(H, \vec{x}) \cdot P_{x|H,x}(x_+|H, \vec{x}) P_{H|x}(H|\vec{x})}{P_x(\vec{x}) P_H(H) \cdot P_{x|x}(x_+|\vec{x}) P_{H|x}(H|\vec{x})} \quad (\text{A32})$$

$$I(H; \vec{x}, x_+) = I(H; \vec{x}) + I(H; x_+|\vec{x}). \quad (\text{A33})$$

As mentioned in Appendix A 2a, an application of the Gibb's inequality makes it easy to show both $I(a; b) \geq 0$ and $I(a; b|c) \geq 0$. Thus we have

$$I(H; \vec{x}, x_+) \geq I(H; \vec{x}) \quad (\text{A34})$$

which proves that adding a search statistic can only add to the mutual information, and thus it can only decrease

$$\begin{aligned} P_{x|H_{\text{bin}}}(\vec{x}|H_{\text{pos}}) &= \sum_i P_{x|H, H_{\text{bin}}}(\vec{x}|H_i, H_{\text{pos}}) P_{H|H_{\text{bin}}}(H_i|H_{\text{pos}}) \\ &= P_{x|H, H_{\text{bin}}}(\vec{x}|H_0, H_{\text{null}}) \\ &\quad \cdot \sum_{H_i \in H_{\text{pos}}} \Lambda_{i,0}(\vec{x}) P_{H|H_{\text{bin}}}(H_i|H_{\text{pos}}) \end{aligned} \quad (\text{A30})$$

By defining $a(\vec{\Lambda}(\vec{x}), H_{\text{bin}})$ to be the correct positive-versus-null hypothesis summation term and $b(\vec{x}) = P_{x|H, H_{\text{bin}}}(\vec{x}|H_0, H_{\text{null}})$, we complete the Neyman-Fisher factorization and show that $\vec{\Lambda}(\vec{x})$ is a sufficient statistic with respect to the information contained within \vec{x} about H_{bin} in addition to being a sufficient statistic with respect to H . Thus, if we further losslessly compress $\vec{\Lambda}(\vec{x})$ into a single, scalar search statistic $\Lambda_{\text{bin}}(\vec{\Lambda}(\vec{x}))$, we have not lost any information about H_{bin} . This is an important result. It shows that we can achieve lossless data compression into a scalar in two ways: 1.) directly into Λ_{bin} from the data vector \vec{x} , or 2.) first into a set of likelihood ratios spanning a set of embedded sub-hypotheses and then into Λ_{bin} .

d. Adding Search Statistics can only Increases Information

As discussed above, any vector of search statistics \vec{x} contains a non-negative amount of information $I(H; \vec{x})$ about a hypothesis H . Eq. A10 demonstrates that this mutual information can be interpreted as the reduction in entropic uncertainty of H achieved by having knowledge of the search statistics \vec{x} . It is interesting to study what happens to the mutual information when we change the dimension of \vec{x} , i.e., what happens when we add or remove a given search statistic from our vector. We can consider the mutual information with an added search statistic x_+ by explicitly writing out $I(H; \vec{x}, x_+)$ and factoring the probabilities:

$$I(H; \vec{x}, x_+) = \sum_{H, x, x_+} P_{H,x}(H, \vec{x}, x_+) \log \frac{P_{H,x}(H, \vec{x}, x_+)}{P_x(\vec{x}, x_+) P_H(H)} \quad (\text{A31})$$

$$I(H; \vec{x}, x_+) = \sum_{H, x, x_+} P_{H,x}(H, \vec{x}, x_+) \log \frac{P_{H,x}(H, \vec{x}) \cdot P_{x|H,x}(x_+|H, \vec{x}) P_{H|x}(H|\vec{x})}{P_x(\vec{x}) P_H(H) \cdot P_{x|x}(x_+|\vec{x}) P_{H|x}(H|\vec{x})} \quad (\text{A32})$$

the entropic uncertainty $\mathcal{H}(H|\vec{x})$ of that hypothesis. In other words, adding a search statistic can only make $P_{H|x}(H|\vec{x})$ a more sharply-peaked distribution.

e. Bayes Factors as Sufficient Statistics

Here we note that both of the Bayes factors, BSN and BCI, take the form of likelihood ratios, and thus they

can be treated as sufficient statistics in certain scenarios. To be precise, the BSN is the ratio of the likelihood of having a coherent sine-Gaussian signal in data streams containing Gaussian noise to the likelihood of having data streams containing only Gaussian noise. The BCI is ratio of the likelihood of having a coherent sine-Gaussian signal in data streams containing Gaussian noise to the likelihood of having incoherent sine-Gaussian noise artifacts in data streams containing Gaussian noise. Thus, if GW signals take the form of a sine-Gaussians and the detector noise is only Gaussian, the BSN is a sufficient statistic and preserves all of the information contained within the data streams about the detection hypothesis. Likewise, if GW signals take the form of sine-Gaussians and the detector noise is Gaussian with incoherent sine-Gaussian noise artifacts, the BCI is a sufficient statistic and preserves all of the information contained within the data streams about the detection hypothesis.

Furthermore, as shown in Appendix A 2 c, the set of Bayes factors $\vec{B} = \{\text{BSN}, \text{BCI}\}$ is a sufficient statistic for a 3-dimensional hypothesis test, where the hypotheses are: 1.) a coherent sine-Gaussian signal in data streams containing Gaussian noise, 2.) incoherent sine-Gaussian noise artifacts in data streams containing Gaussian noise, and 3.) data streams containing only Gaussian noise. Thus, if GW signals take the form of sine-Gaussians and the detector noise is either only Gaussian *or* is Gaussian with incoherent sine-Gaussian noise artifacts, then *both* \vec{B} and the likelihood ratio $\Lambda_{\text{bin}}(\vec{B})$ are sufficient statistics and preserve all of the information contained within the data streams about the signal-versus-noise binary hypothesis.

Nevertheless, the above models are expected to be approximations to the actual detection scenarios. We do not expect the detector data streams to contain only Gaussian noise, nor do we expect GW signals and noise artifacts to be perfect sine-Gaussians. These modeling errors will cause information for triggers to be lost when compressing the data into a set of Bayes factors. It is clear from both Appendix A 2 c and Appendix A 2 d that adding Bayes factors as search statistics can only add to the amount of information contained within $\Lambda_{\text{bin}}(\vec{B})$, and that if a Bayes factor describing the true hypotheses is added, this information is maximal. Thus, any improvements to the set of Bayes factors that are used as search statistics, either through the addition of more hypotheses or through the use of better-modeled hypotheses, can only improve upon the ability to distinguish signals from noise.

Appendix B: Gaussian Kernel Density Estimation

In order for us to use an LRT for our signal-versus-noise binary hypothesis test, we need models of the signal and noise likelihoods. Without a given functional form for these likelihood distributions, we must find a way of approximating them in some optimal sense. The

Kullback-Leibler divergence between two distributions P and Q , defined as

$$D(P||Q) = \sum_i P(i) \log \frac{P(i)}{Q(i)}, \quad (\text{B1})$$

provides a measure of the distance between two distributions. It represents the reduction in entropy when using the true distribution P instead of the wrong distribution Q , or in an information-theoretic sense, it measures the loss of information when using the wrong distribution Q instead of the true distribution P . Thus, if we wish to model the true distribution $f(\vec{x})$ of our search statistics \vec{x} with a model distribution $\hat{f}(\vec{x})$, we should minimize $D(f||\hat{f})$ in order to maximize the information that is contained within $\hat{f}(\vec{x})$ about \vec{x} . By changing the sum in Eq. B1 to an integral in order to account for continuous variables, the quantity to be minimized becomes

$$D(f||\hat{f}) = \int f(\vec{x}) \log f(\vec{x}) d\vec{x} - \int f(\vec{x}) \log \hat{f}(\vec{x}) d\vec{x}. \quad (\text{B2})$$

Since only the second term in Eq. B2 depends on our model choice $\hat{f}(\vec{x})$, the optimization problem becomes a maximization of

$$B = \int f(\vec{x}) \log \hat{f}(\vec{x}) d\vec{x}. \quad (\text{B3})$$

With our optimization criterion in place, we must then choose our model $\hat{f}(\vec{x})$. One non-parametric approach to this problem is that of kernel density estimation (KDE). KDE consists of centering an N -dimensional kernel at each of a set of N -dimensional empirical data points drawn from $f(\vec{x})$. These kernels are then summed over, and the normalized sum is used as the distribution model $\hat{f}(\vec{x})$. When identical Gaussian kernels are used for each data point, this model takes the form

$$\hat{f}(\vec{x}) = \frac{1}{n \sqrt{(2\pi)^N |H|}} \sum_i^n e^{-\frac{1}{2}(\vec{x} - \vec{d}_i)^\top H^{-1}(\vec{x} - \vec{d}_i)} \quad (\text{B4})$$

where i indexes one of n data points drawn from the true distribution $f(\vec{x})$ and H is a matrix representing the squared bandwidths of the kernels. A kernel's bandwidth h_m controls the width of the kernel (i.e., the extent to which it models local versus distant parts of the parameter space) in the m^{th} dimension. If we choose all of the N bandwidths (one for each dimension) to be uncorrelated, then H is a diagonal matrix with h_m^2 as the m^{th} entry along the diagonal.

In order to evaluate Eq. B3, we need to know the functional form of $f(\vec{x})$. We can approximate this using the empirical approximation

$$\int f(\vec{x}) g(\vec{x}) d\vec{x} = E_f[g(\vec{x})] \approx \frac{1}{n} \sum_j^n g(\vec{d}_j) \quad (\text{B5})$$

where we replace the integral over \vec{x} with a sum over the n data points $\vec{d}_1, \dots, \vec{d}_n$ sampled from $f(\vec{x})$. For our

purposes, $g(\vec{x}) = \log \hat{f}(\vec{x})$, giving us

$$B \approx \frac{1}{n} \sum_j^n \log \left(\frac{1}{n \sqrt{(2\pi)^N |H|}} \sum_i^n e^{-\frac{1}{2}(\vec{d}_j - \vec{d}_i)^\top H^{-1}(\vec{d}_j - \vec{d}_i)} \right). \quad (\text{B6})$$

Finally, in order to prevent ourselves from overtraining the data, we use leave-one-out cross-validation by removing the j^{th} data point from the inner sum, yielding the expression

$$B \approx \frac{1}{n} \sum_j^n \log \left(\frac{1}{(n-1) \sqrt{(2\pi)^N |H|}} \sum_{i \neq j}^n e^{-\frac{1}{2}(\vec{d}_j - \vec{d}_i)^\top H^{-1}(\vec{d}_j - \vec{d}_i)} \right). \quad (\text{B7})$$

The result of overtraining can be seen by considering the case where $H \rightarrow \mathbf{0}$. In this limit, all of the Gaussian Kernels become Dirac delta functions centered around d_j . Thus, the $i = j$ point provides an infinite contribution to B , meaning a zero-bandwidth KDE is optimal and that the optimal estimate of $f(\vec{x})$ is simply the set of empirical data points. Removing the $i = j$ point from the sum helps prevent this overtraining, although it should be noted that the zero-bandwidth B will be infinite and therefore maximal if any of the data points are duplicates (which becomes more and more unlikely as the dimensionality N increases).

In practice, we find the optimal bandwidths of our KDE likelihood estimates by maximizing Eq. B7 over a grid in the N -dimensional parameter space. In cases where the zero bandwidth is infinite, we search instead for a secondary local maximum.

Appendix C: Distributions of LIB Runtimes

Because the calculation of the Bayes factors requires LIB to integrate the entirety of parameter space of a GW signal model, it is the most computationally expensive step in the oLIB pipeline. Executing the Omicron, incoherent down-selection, and likelihood-ratio steps all take place on the timescales of a few tens of seconds. As

Fig. 10 and Table VI demonstrate, the lower limit of the LIB timescale is a few hundreds of seconds. We emphasize that background triggers represent a lower limit to the timescale because they have a more diffuse likelihood distribution, which LIB can integrate more quickly than the more sharply peaked distributions associated with coherent GW signals.

It should be noted that the LIB timescale for GW signals is a few thousands of seconds. This property helps explain the runtime distributions shown in Fig. 10. The right tails of the distributions can be attributed to the most signal-like background event triggers. The set of background events with a lower-network-SNR threshold of $6.5\sqrt{2}$ consisted of a larger percentage of high-BSN event triggers than did the set with a lower SNR threshold of $5.5\sqrt{2}$, explaining the longer right tails for the $6.5\sqrt{2}$ -thresholded set. That the average runtimes were longer for L1 than for H1 is consistent with the incoherent analysis of III A, which shows that L1 contained a greater number of high-SNR triggers than H1. Finally, LIB took longer to run jointly over both detector's data streams than it did to run over each detector's data streams individually because the constraint that signals should be coherent in both detectors makes it easier to distinguish between signal and noise, causing the likelihood distributions to become more sharply peaked [27].

TABLE VI. The mean and median runtimes for the LIB background analyses searching both coherently in the two detectors (H1L1), and incoherently in the individual detectors (H1 and L1). The runtime statistics are given independently for the background sets with lower-network-SNR thresholds of $5.5\sqrt{2}$ and $6.5\sqrt{2}$.

Run type	H1L1		H1		L1	
	Mean runtime (s)	Median runtime (s)	Mean runtime (s)	Median runtime (s)	Mean runtime (s)	Median runtime (s)
Network SNR threshold of $5.5\sqrt{2}$	439	376	187	178	202	174
Network SNR threshold of $6.5\sqrt{2}$	1148	1107	205	177	569	539

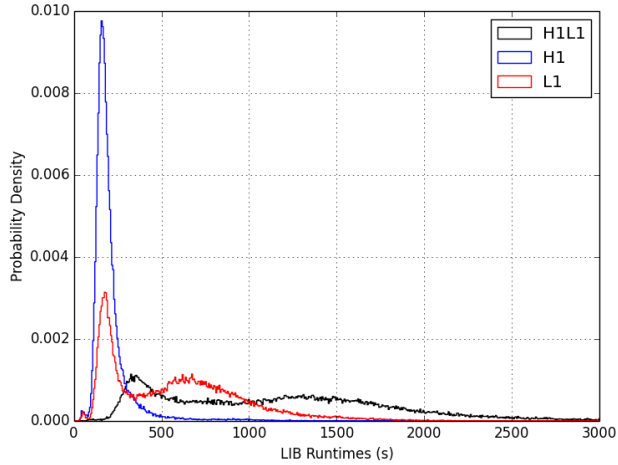
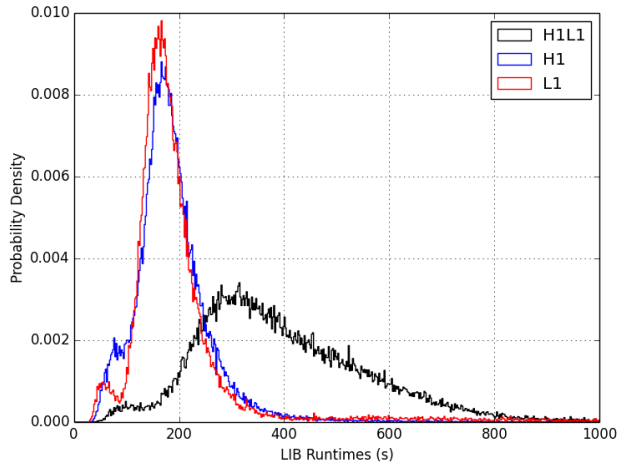


FIG. 10. The distribution of LIB runtimes for background events. LIB analyzed the data either with a single detector (H1 or L1) or coherently across both detectors (H1L1). The top and bottom plots show the distributions the background sets with lower-network-SNR thresholds of $5.5\sqrt{2}$ and $6.5\sqrt{2}$, respectively.